Titre: Title:	Generic acquisition protocol for quantitative MRI of the spinal cord
Auteurs: Authors:	Julien Cohen-Adad, Eva Alonso Ortiz, Mihael Abramovic, Carina Arneitz, Nicole Atcheson, Laura Barlow, Robert L. Barry, Markus Barth, Marco Battiston, Christian Büchel, Matthew Budde, Virginie Callot, Anna J. E. Combes, Benjamin De Leener, Maxime Descoteaux, Paulo Loureiro de Sousa, Marek Dostál, Julien Doyon, Adam Dvorak, Falk Eippert, Karla R. Epperson, Kevin S. Epperson, Patrick Freund, Jürgen Finsterbusch, Alexandru Foias, Michela Fratini, Issei Fukunaga, Claudia Angela M. Gandini Wheeler-Kingshott, Giancarlo Germani, Guillaume Gilbert, Federico Giove, Charley Gros, Francesco Grussu, Akifumi Hagiwara, Pierre-Gilles Henry, Tomáš Horák, Masaaki Hori, James Joers, Kouhei Kamiya, Haleh Karbasforoushan, Miloš Keřkovský, Ali Khatibi, Joo-Won Kim, Nawal Kinany, Hagen Kitzler, Shannon Kolind, Yazhuo Kong, Petr Kudlička, Paul Kuntke, Nyoman D. Kurniawan, Slawomir Kusmia, René Labounek, Maria Marcella Laganà, Cornelia Laule, Christine S. Law, Christophe Lenglet, Tobias Leutritz, Yaou Liu, Sara Llufriu, Sean Mackey, Eloy Martinez-Heras, Loan Mattera, Igor Nestrasil, Kristin P. O'Grady, Nico Papinutto, Daniel Papp, Deborah Pareto, Todd B. Parrish, Anna Pichiecchio, Ferran Prados, Àlex Rovira, Marc J. Ruitenberg, Rebecca S. Samson, Giovanni Savini, Maryam Seif, Alan C. Seifert, Alex K. Smith, Seth A. Smith, Zachary A. Smith, Elisabeth Solana, Yuichi Suzuki, George Tackley, Alexandra Tinnermann, Jan Valošek, Dimitri Van De Ville, Marios C. Yiannakas, Kenneth A. Weber, Nikolaus Weiskopf, Richard G. Wise, Patrik O. Wyss, & Junqian Xu
Date:	2021
Type:	Article de revue / Article
Référence: Citation:	Cohen-Adad, J., Alonso Ortiz, E., Abramovic, M., Arneitz, C., Atcheson, N., Barlow, L., Barry, R. L., Barth, M., Battiston, M., Büchel, C., Budde, M., Callot, V., Combes, A. J. E., De Leener, B., Descoteaux, M., de Sousa, P. L., Dostál, M., Doyon, J., Dvorak, A., ... Xu, J. (2021). Generic acquisition protocol for quantitative MRI of the spinal cord. Nature Protocols, 16(10), 4611-4632. https://doi.org/10.1038/s41596-021-00588-0

Version:	Version finale avant publication / Accepted version Révisé par les pairs / Refereed
Conditions d'utilisation: Terms of Use:	Tous droits réservés / All rights reserved

Document publié chez l'éditeur officiel
Document issued by the official publisher

Titre de la revue: Journal Title:	Nature Protocols (vol. 16, no. 10)
Maison d'édition: Publisher:	Springer Nature
URL officiel: Official URL:	https://doi.org/10.1038/s41596-021-00588-0
Mention légale: Legal notice:	This version of the article has been accepted for publication, after peer review (when applicable) and is subject to Springer Nature's AM terms of use, but is not the Version of Record and does not reflect post-acceptance improvements, or any corrections. The Version of Record is available online at: https://doi.org/10.1038/s41596-021-00588-0

Generic acquisition protocol for quantitative MRI of the spinal cord

Julien Cohen-Adad[1,2,3], Eva Alonso-Ortiz[1], Mihael Abramovic[4], Carina Arneitz[4], Nicole Atcheson[5], Laura Barlow[6], Robert L. Barry[7,8,9], Markus Barth[10], Marco Battiston[11], Christian Büchel[12], Matthew Budde[13], Virginie Callot[14,15], Anna J.E. Combes[16], Benjamin De Leener[17,18], Maxime Descoteaux[19,20], Paulo Loureiro de Sousa[21], Marek Dostál[22], Julien Doyon[23], Adam Dvorak[24], Falk Eippert[25], Karla R. Epperson[26], Kevin S. Epperson[26], Patrick Freund[27], Jürgen

---

[1] NeuroPoly Lab, Institute of Biomedical Engineering, Polytechnique Montreal, Montreal, QC, Canada
[2] Functional Neuroimaging Unit, CRIUGM, University of Montreal, Montreal, QC, Canada.
[3] Mila - Quebec AI Institute, Montreal, QC, Canada
[4] Department of Radiology, Swiss Paraplegic Centre, Nottwil, Switzerland
[5] Centre for Advanced Imaging, The University of Queensland, Brisbane, Australia
[6] Department of Radiology, University of British Columbia, Vancouver, BC, Canada
[7] Athinoula A. Martinos Center for Biomedical Imaging, Department of Radiology, Massachusetts General Hospital, Charlestown, MA, USA
[8] Department of Radiology, Harvard Medical School, Boston, MA, USA
[9] Harvard–Massachusetts Institute of Technology Health Sciences & Technology, Cambridge, MA, USA
[10] School of Information Technology and Electrical Engineering, The University of Queensland, Brisbane, Australia
[11] NMR Research Unit, Queen Square MS Centre, UCL Queen Square Institute of Neurology, Faculty of Brain Sciences, University College London, London, United Kingdom
[12] Department of Systems Neuroscience, University Medical Center Hamburg-Eppendorf, Hamburg, Germany
[13] Department of Neurosurgery, Medical College of Wisconsin, Milwaukee, WI, USA
[14] Aix-Marseille Univ, CNRS, CRMBM, Marseille, France
[15] APHM, Hopital Universitaire Timone, CEMEREM, Marseille, France
[16] Vanderbilt University Institute of Imaging Science, Vanderbilt University Medical Center, Nashville, TN, USA
[17] Department of Computer and Software Engineering, Polytechnique Montreal, Montreal Canada
[18] CHU Sainte-Justine Research Centre, Montreal, QC, Canada
[19] Centre de Recherche CHUS, CIMS, Sherbrooke, Canada
[20] Sherbrooke Connectivity Imaging Lab (SCIL), Computer Science department, Université de Sherbrooke
[21] Université de Strasbourg, CNRS, ICube, Strasbourg, France
[22] UHB - University Hospital Brno and Masaryk University, Department of Radiology and Nuclear Medicine, Czech Republic
[23] McConnell Brain Imaging Centre, Montreal Neurological Institute, McGill University, Montreal, QC, Canada
[24] Department of Physics and Astronomy, University of British Columbia, Vancouver, BC, Canada
[25] Max Planck Institute for Human Cognitive and Brain Sciences, Leipzig, Germany
[26] Richard M. Lucas Center, Stanford University School of Medicine, Stanford, CA USA
[27] Spinal Cord Injury Center Balgrist, University of Zurich, Switzerland

Finsterbusch[12], Alexandru Foias[1], Michela Fratini[28,29], Issei Fukunaga[30], Claudia A.M. Gandini Wheeler-Kingshott[11,31,32], Giancarlo Germani[32], Guillaume Gilbert[33], Federico Giove[34,29], Charley Gros[1,5], Francesco Grussu[11,35], Akifumi Hagiwara[30], Pierre-Gilles Henry[36], Tomáš Horák[37], Masaaki Hori[38], James Joers[36], Kouhei Kamiya[39], Haleh Karbasforoushan[40,41], Miloš Keřkovský[22], Ali Khatibi[23,42], Joo-Won Kim[43], Nawal Kinany[44,45], Hagen Kitzler[46], Shannon Kolind[6,24,47], Yazhuo Kong[48,49,50], Petr Kudlička[37], Paul Kuntke[46], Nyoman D. Kurniawan[5], Slawomir Kusmia[51,52,53],

[28] Institute of Nanotechnology, CNR, Rome, Italy

[29] IRCCS Santa Lucia Foundation, Rome, Italy

[30] Department of Radiology, Juntendo University School of Medicine, Tokyo, Japan

[31] Department of Brain and Behavioural Sciences, University of Pavia, Pavia, Italy

[32] Brain MRI 3T Research Centre, IRCCS Mondino Foundation, Pavia, Italy

[33] MR Clinical Science, Philips Healthcare, Markham, ON, Canada

[34] CREF - Museo storico della fisica e Centro studi e ricerche Enrico Fermi, Rome, Italy

[35] Radiomics Group, Vall d'Hebron Institute of Oncology, Vall d'Hebron Barcelona Hospital Campus, Barcelona, Spain

[36] Center for Magnetic Resonance Research, Department of Radiology, University of Minnesota, Minneapolis, MN, USA

[37] Multimodal and functional imaging laboratory, Central European Institute of Technology (CEITEC), Brno, Czech Republic

[38] Department of Radiology, Toho University Omori Medical Center, Tokyo, Japan

[39] Department of Radiology, the University of Tokyo, Tokyo, Japan

[40] Interdepartmental Neuroscience Program, Feinberg School of Medicine, Northwestern University, Chicago, IL, USA

[41] Department of Psychiatry and Behavioral Sciences, School of Medicine, Stanford University, Stanford, CA, USA

[42] Centre of Precision Rehabilitation for Spinal Pain (CPR Spine), School of Sport, Exercise and Rehabilitation Sciences, College of Life and Environmental Sciences, University of Birmingham, Edgbaston, Birmingham, United Kingdom

[43] BioMedical Engineering and Imaging Institute (BMEII), Department of Radiology, Icahn School of Medicine at Mount Sinai, New York, NY, USA

[44] Institute of Bioengineering/Center for Neuroprosthetics, Ecole Polytechnique Fédérale de Lausanne, Geneva, Switzerland

[45] Department of Radiology and Medical Informatics, University of Geneva, Geneva, Switzerland

[46] Institute of Diagnostic and Interventional Neuroradiology, Carl Gustav Carus University Hospital, Technische Universität Dresden, Dresden, Germany

[47] Department Of Medicine (Neurology), University of British Columbia, Vancouver, BC, Canada

[48] CAS Key Laboratory of Behavioral Science, Institute of Psychology, Chinese Academy of Sciences, Beijing, China

[49] Department of Psychology, University of Chinese Academy of Sciences, Beijing, China

[50] Wellcome Centre For Integrative Neuroimaging, FMRIB, Nuffield Department of Clinical Neurosciences, University of Oxford, Oxford, United Kingdom

[51] CUBRIC, Cardiff University, Wales, UK

[52] Centre for Medical Image Computing (CMIC), Medical Physics and Biomedical Engineering Department, University College London, London, United Kingdom

[53] Epilepsy Society MRI Unit, Chalfont St Peter, United Kingdom

René Labounek[54,55], Maria Marcella Laganà[56], Cornelia Laule[57], Christine S. Law[58], Christophe Lenglet[36], Tobias Leutritz[59], Yaou Liu[60,61], Sara Llufriu[62], Sean Mackey[58], Eloy Martinez-Heras[62], Loan Mattera[63], Igor Nestrasil[36,54], Kristin P. O'Grady[16,64], Nico Papinutto[65], Daniel Papp[1,50], Deborah Pareto[66], Todd B. Parrish[40], Anna Pichiecchio[31,32], Ferran Prados[11,52,67], Àlex Rovira[66], Marc J. Ruitenberg[68], Rebecca S. Samson[11], Giovanni Savini[32], Maryam Seif[27,59], Alan C. Seifert[43], Alex K. Smith[50], Seth A. Smith[16,64], Zachary A. Smith[69], Elisabeth Solana[62], Y. Suzuki[39], George Tackley[51], Alexandra Tinnermann[12], Jan Valošek[70], Dimitri Van De Ville[44,45], Marios C. Yiannakas[11], Kenneth A. Weber II[58], Nikolaus Weiskopf[59,71], Richard G. Wise[51,72], Patrik O. Wyss[4], Junqian Xu[43]

[54] Division of Clinical Behavioral Neuroscience, Department of Pediatrics, University of Minnesota, Minneapolis, MN, USA

[55] Departments of Neurology and Biomedical Engineering, University Hospital Olomouc, Olomouc, Czech Republic

[56] IRCCS Fondazione Don Carlo Gnocchi ONLUS, Milan, Italy

[57] Departments of Radiology, Pathology & Laboratory Medicine, Physics & Astronomy; International Collaboration on Repair Discoveries (ICORD), University of British Columbia, Vancouver, BC, Canada

[58] Division of Pain Medicine, Department of Anesthesiology, Perioperative and Pain Medicine, Stanford University School of Medicine, Stanford, CA, USA

[59] Department of Neurophysics, Max Planck Institute for Human Cognitive and Brain Sciences, Leipzig, Germany

[60] Department of Radiology, Beijing Tiantan Hospital, Capital Medical University, Beijing, China

[61] Tiantan Image Research Center, China National Clinical Research Center for Neurological Diseases, Beijing, China

[62] Center of Neuroimmunology, Laboratory of Advanced Imaging in Neuroimmunological Diseases, Hospital Clinic Barcelona, Institut d'Investigacions Biomèdiques August Pi i Sunyer (IDIBAPS) and Universitat de Barcelona, Barcelona, Spain

[63] Fondation Campus Biotech Genève, 1202, Geneva, Switzerland

[64] Department of Radiology, Vanderbilt University Medical Center, Nashville, TN USA

[65] UCSF Weill Institute for Neurosciences, Department of Neurology, University of California San Francisco, San Francisco, CA, USA

[66] Neuroradiology Section, Vall d'Hebron University Hospital, Barcelona, Spain

[67] E-health Centre, Universitat Oberta de Catalunya, Barcelona, Spain

[68] School of Biomedical Sciences, Faculty of Medicine, The University of Queensland, Brisbane, Australia

[69] University of Oklahoma Health Sciences Center, Oklahoma City, OK, USA

[70] Department of Neurology, Faculty of Medicine and Dentistry, Palacký University and University Hospital Olomouc, Olomouc, Czech Republic

[71] Felix Bloch Institute for Solid State Physics, Faculty of Physics and Earth Sciences, Leipzig University, Leipzig, Germany

[72] Institute for Advanced Biomedical Technologies, Department of Neuroscience, Imaging and Clinical Sciences, "G. D'Annunzio University" of Chieti-Pescara, Italy

Abstract

Quantitative spinal cord (SC) magnetic resonance imaging (MRI) presents many challenges, including a lack of standardized imaging protocols. Here we present a prospectively harmonized quantitative MRI protocol, which we refer to as the *spine generic* protocol, for users of 3T MRI systems from the three main manufacturers: GE, Philips and Siemens. The protocol provides guidance for assessing SC macrostructural and microstructural integrity: T1-weighted and T2-weighted imaging for SC cross-sectional area (CSA) computation, multi-echo gradient echo for gray matter CSA, and magnetization transfer and diffusion weighted imaging for assessing white matter microstructure. In a companion paper from the same authors, the *spine generic* protocol was used to acquire data across 42 centers in 260 healthy subjects. The key details of the *spine generic* protocol are also available in an open-access document that can be found at: https://spinalcordmri.org/protocols. The protocol will serve as a starting point for researchers and clinicians implementing new SC imaging initiatives so that, in the future, inclusion of the SC in neuroimaging protocols will be more common. The protocol could be implemented by any trained MR technician or by a researcher/clinician familiar with MRI acquisition.

Introduction

Quantitative MRI (qMRI) aims to provide objective continuous metrics that specifically reflect the morphology, microstructure and/or chemical composition of tissues [1,2], thereby enabling deeper insight and understanding of disease pathophysiology. While qMRI techniques have been successfully implemented in the brain for several decades, they remain largely underutilized for spinal cord (SC) imaging in both clinical and research settings, mostly as a direct consequence of the many challenges that need to be overcome in order to acquire good quality data [3,4].

For the past 20 years, researchers have been developing methods to overcome the challenges around SC imaging, including more sensitive coil arrays [5,6] and advanced pulse sequences for mitigating motion and susceptibility artifacts [4,7]. As a result, it is now possible to acquire SC qMRI data that have a strong potential for providing new insights into SC anatomy and function. However, a remaining issue is that there is no clear consensus within the imaging community for acquiring SC qMRI data, leading to (i) wasted time and money spent on pilot scans for every new SC research initiative, and (ii) large variability in imaging parameters for multi-site, multi-manufacturer studies, hampering statistics for assessing biomarkers.

Development of the Protocol

The present study gathered a consortium of international SC researchers to provide a prospectively harmonized consensus protocol for acquiring high-quality qMRI of the human cervical SC at 3 Tesla (T) across the three main MRI manufacturers (GE, Philips and Siemens). We call this the *spine generic* protocol. QMRI techniques covered in the *spine generic* protocol (illustrated in **Figure 1**) include:

SC cross-sectional area (CSA): The CSA of the whole SC has been shown to be a sensitive biomarker in multiple sclerosis (MS) [8–11], amyotrophic lateral sclerosis (ALS) [12–16], X-linked adrenoleukodystrophy (ALD) with myelopathy[17], as well as both traumatic and non-traumatic SC injury [18,19]. Additionally, SC segmentation is useful for atlas-based analysis [20].

CSA of the SC gray matter (GM): GM CSA is relevant for diagnosis [21] and prognosis in ALS [16]. Additionally, delineating the GM is relevant for quantifying pathologies juxtaposed with the GM (e.g. MS lesions), for fMRI applications, and for atlas-based analysis.

Diffusion tensor imaging (DTI): DTI is a technique that is based on multi-directionally encoded diffusion weighted images (DWI). DTI can quantify microstructural integrity and has been deemed sensitive to degeneration and demyelination of SC white matter (WM) tracts in a variety of diseases[3,22–25] and after SC injury[19,23]. In non-traumatic SC injury, DWI appears to be a promising approach that is sensitive to presymptomatic microstructural changes[26,27].

Magnetization transfer (MT): The MT technique has been shown to be sensitive to demyelination [28] and has been applied in various SC diseases, such as adrenomyeloneuropathy (AMN) [29] and MS [30], as well as in SC injury [22,31].
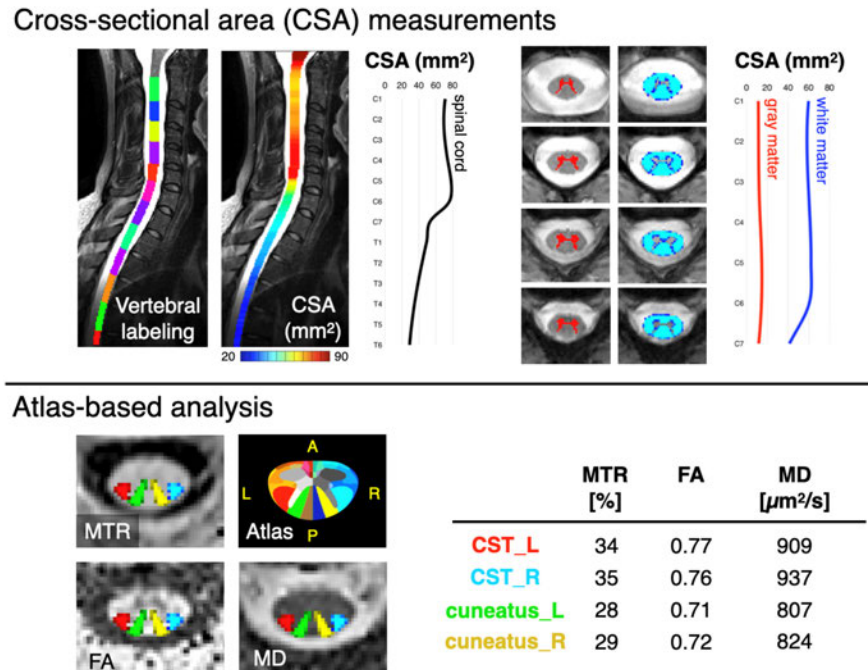
Figure 1. Illustration of the MRI metrics that could be extracted from the spine generic protocol. The top panel "Cross-sectional area (CSA) measurements" shows morphometric measures of the spinal cord and its gray and white matter. The bottom panel "Atlas-based analysis" on the left shows axial views of qMRI maps: Magnetization Transfer Ratio (MTR), Fractional Anisotropy (FA) and Mean Diffusivity (MD), with an overlay of 4 spinal tracts of general interest: the descending corticospinal tract (CST) and the ascending cuneatus, left (L) and right (R). The "Atlas" image corresponds to the white matter atlas [32], which includes 30 white matter tracts that could be used for computing metrics within specific tracts of interest. This atlas also includes 6 parcellations of the gray matter. The table shows average values of each metric in the corresponding tract.

To demonstrate the practical implementation and reproducibility of the proposed protocol, single-subject and multi-subject datasets were acquired across multiple centers. Relevant qMRI metrics were calculated using a fully-automatic analysis pipeline, and those metrics were compared within site, across sites (for the same manufacturer), and across different manufacturers. Details of the datasets, processing pipelines and generated normative values are available in a companion Data Descriptor paper published in Scientific Data [33].

When optimizing protocols across manufacturers, a key question is: *Should we minimize the differences in acquisition parameters across manufacturers, or should we optimize image quality on each platform?* The *spine generic* protocol was designed to reach a compromise between these two key aims: minimizing protocol differences in order to facilitate the interpretation of multi-manufacturer studies, but at the same time we optimized parameters for each manufacturer separately when the hardware or software enabled it. For example, on the DWI protocol, the echo time (TE) was always minimized in order to maximize SNR, which minimally affects the diffusion-specific signal (the b-value was kept the same). Given that platforms are equipped with different

gradient nominal strength capabilities (ranging from 40 mT/m to 80 mT/m for current clinical systems), this yielded very different TEs depending on the platform. These aspects were taken into consideration when designing the spine generic protocol, resulting in a protocol with a high SNR regime that is hence less sensitive to changes in the TE. As illustrated in the companion data paper [33], fractional anisotropy values across Siemens sites equipped with gradient systems varying from 40 to 80 mT/m (TEs ranging from 55 to 99 ms), produced an inter-site coefficient of variation (COV) of 3.5%, which was smaller than the intra-site COV of 4.24%. The intersubject variability was thus higher than the inter-site variability, despite the large changes in TEs. Another important consideration is that different TE across manufacturers/models will likely result in different diffusion times. This may be an additional source of inter-manufacturer variability, as it has been shown that common DWI metrics such as DTI radial diffusivity can exhibit diffusion time dependence, especially in anatomical regions containing large axons [34]. Similarly, some software versions were limited with respect to the minimum achievable repetition time (TR) on MT sequences; again, here the TR was optimized for each system separately, yielding full MT protocols (GRE-MT1/MT0/T1w) that varied from 5.4 min to 8.9 min, depending on the platform. However, in this case, MTR and MTsat were impacted by TR. This partly explains the discrepancies observed between GE and the two other manufacturers (see [33]).

Because hardware and pulse sequence environments vary across manufacturers, it will never be possible to obtain the exact same acquisition configuration across manufacturers. Even for the same manufacturer, some variability could exist due to the different specifications for different models and the adjustment and maintenance status of individual scanners (acoustic resonances, helium levels, eddy-currents, software patches, etc.). From a practical standpoint, as in the case for the T1w vs. T2w SC CSA (see Figure 11 in [33]), the relationship between qMRI metrics obtained from different manufacturers/models/sites can be modeled as fixed or random effects [35].

The *spine generic* protocol has been used (fully, in part or with modifications) in the following applications: imaging methods [36], method development in healthy subjects [20,37–50], functional MRI [51,52], MS [53–55], mucopolysaccharidoses [56], adrenoleukodystrophy[17], ALS [16,57], spinal muscular atrophy [58,59], degenerative cervical myelopathy [26,27,60–62], and stroke [63].

The *spine generic* protocol has also been recommended in recent guidelines[24,64–67] and was adopted by multi-center initiatives such as the INSPIRED[68] and the CanProCo[55] studies, respectively dealing with cervical myelopathy and MS populations.

Applications

The proposed protocol is not geared towards a specific disease and it is suitable for imaging WM pathology (demyelination and Wallerian degeneration via axon/myelin-sensitive techniques), GM pathology (ALS, via GM CSA quantification), and traumatic and non-traumatic SC injury (structural scans to assess compression and/or to quantify atrophy above/below lesions or injury). Additional clinical scans (e.g. 2D FLAIR, STIR) that are specific to particular diseases and/or are part of the clinical routine can be added at the discretion of the researcher/clinician. Potential clinical uses of this protocol include improved diagnosis of pathology, monitoring of disease progression or recovery, and/or prediction of outcomes.

Experimental Design

Sequences

The required sequences are illustrated in **Figure 2**. Justifications for the sequence type and their pros and cons are summarized in **Table 1**. The manufacturer-specific sequence names are listed in **Table 2**.

Table 1. Purpose, pros and cons of sequences of the spine generic protocol.			
	Purpose	**Pros**	**Cons**
T1w (3D sagittal)	- Measuring SC CSA and/or volume - Registering to a template (preferred for disc labeling) - Assessing lesions - Measuring brain atrophy	- Efficient SNR per unit time - High SC/CSF contrast (good for SC segmentation) - $320\ mm^2$ FOV in ~5min at 1 mm iso with full brain and cervical-spine coverage - Low specific absorption rate (SAR) - High WM/GM contrast in the brain (good for cortical surface segmentation) - Vertebral discs are well contrasted	- Sensitive to motion (pulsatile, swallowing) - Poor WM/GM contrast in the SC
T2w (3D sagittal)	- Measuring SC CSA and/or volume (preferred over the 3D T1w due to higher spatial resolution) - Registering to a template registration (preferred for cord segmentation) - Assessing lesions and compression	- Very high SC/CSF contrast - Less sensitive to motion than the 3D T1w - Better spatial resolution than the 3D T1w (0.8 mm vs. 1 mm)	- High SAR - Poor WM/GM contrast in the SC - Cannot cover full brain in <10 min at 0.8 mm iso - Poor visibility of vertebral discs - More prone to Gibbs ringing artifact at high-contrast SC/CSF interface
DWI (2D axial)	- Computing DTI metrics (fractional anisotropy (FA), mean diffusivity (MD), radial diffusivity (RD), axial diffusivity (AD)) that are sensitive to axonal damage, demyelination and degeneration [69].	- Quantify SC neural tissue microstructural properties - Sensitive to WM pathologies (e.g. degenerative demyelination, injury, edema, tumor) - Longitudinal monitoring of patient-specific SC microstructure (i.e. disease progression) - Detect origin of microstructural damage before non-reversible changes (e.g. T2w hyperintensities, appearance of clinical symptoms) - Short acquisition time (<5 min)	- Sensitive to B_0 inhomogeneities (EPI readout) - DTI metrics are biased by SNR [70]

| GRE-MT1/MT0/T1w (3D axial) | - Computing MTR, MT-CSF and MTsat (requires T1w to partially compensate for B1+ homogeneity and T1 effects on the MTR [71])
- Detecting WM [61] and GM pathology (myelopathy) | - Quantify SC neural tissue microstructural properties
- Sensitive to WM pathologies (e.g. degenerative demyelination, injury, edema, tumor)
- Longitudinal monitoring of patient-specific SC microstructure (i.e. disease progression)
- Detect origin of microstructural damage before non-reversible changes (e.g. T2w hyperintensities, appearance of clinical symptoms)
- High in-plane axial resolution (good for atlas-based analysis of various WM tracts)
- The combined echoes provide high WM/GM contrast (depending on parameters).
- Fast
- Low SAR (except for the MT sequence) | - Sensitive to motion
- Sensitive to B_0 inhomogeneities (signal drop-out due to intra-voxel dephasing, can be mitigated using thinner slices)
- Quantitative metrics sensitive to B1 (except for the ME-GRE sequence) |
| ME-GRE (2D axial) | - Segmenting the SC and GM for measuring cord/WM/GM CSA
- Registering to a template and accounting for GM shape
- Measuring SC and GM CSA | | |

Table 2. List of sequences included in the spine generic protocol.

	GE	Philips	Siemens
T1w (3D)	BRAVO/IR-FSPGR	T1TFE	MPRAGE
T2w (3D)	CUBE	VISTA	SPACE
DWI (2D)	Spin Echo EPI with or without FOCUS(*)	Zoom Diffusion(*)	ep2d_diff with or without ZOOMit(*)
ME-GRE (2D)	MERGE	mFFE	GRE "medic"
GRE-MT1/MT0/T1w (3D)	SPGR	FFE	GRE

All sequences come by default with the MRI system, except those marked with (*), which require a special license. ME stands for multi-echo. Note that on the Philips system, the MT1 and MT0 scans are acquired within the same sequence, and the MTR is automatically calculated.

Shimming

Shimming refers to homogenizing the static magnetic field (B_0) and is a necessary step for recording reliable images, especially in regions that are prone to large B_0 inhomogeneities, such as the SC. Without proper shimming, fat saturation would not work effectively, slice excitation

profiles would not be accurate, and EPI data is prone to distortions and signal drop out, with the latter being particularly prevalent in gradient echo imaging often used in functional MRI studies.

The very first "active" attempt to mitigate susceptibility artifacts is usually performed just before starting an MRI scan via a procedure called active shimming. This procedure consists of estimating a field map and then computing a set of "shim coefficients", i.e. the amount of current that needs to go into each gradient and shim coil in order to minimize the static magnetic field inhomogeneity in a specified "shim adjust volume".

Slice orientation

For 3D acquisitions with isotropic resolution (T1w and T2w), we recommend sagittal acquisition for an efficient S-I coverage with the minimum number of slices required to cover the cord (on the T2w). Note that typical clinical 2D scans use thick sagittal slices, which is popular for diagnosis with T1/T2/STIR/PDw contrasts, but these should not be used for measuring CSA or for template-based analysis due to the poor R-L resolution.

For qMRI methods that produce microstructural metrics (MT, DWI), we recommend axial orientation (orthogonal to the SC) with high in-plane resolution and thick slices. This approach takes advantage of the (quasi-) coherently oriented fibers along the S-I direction to increase slice thickness and thus gain SNR. The high in-plane resolution, ideally sub-millimetric, is important for minimizing the partial volume effect between adjacent internal structures (WM tracts, GM), thereby ensuring accurate quantification of metrics. For 2D multislice sequences, if the sequence allows, each individual slice should ideally be orthogonal to the cord [72]. If not possible, slices should be oriented such that the region of most interest is orthogonal to the cord (leaving other regions with larger partial volume effects). Alternatively, if time allows, slices may be separated into several pseudo-contiguous slabs, each orthogonal to the cord and containing 3-5 slices. Note that using thinner slices mitigates the partial volume effect, although this comes at the cost of lower SNR. Thinner slices also mitigate intravoxel dephasing due to inhomogeneities in the static magnetic field, which lead to signal drop-out in gradient-echo imaging [73]. Axial acquisitions with thick slices are also recommended for measuring GM CSA.

Phase-encoding direction

There are a few considerations to be made when choosing the phase-encoding direction. For transverse (perpendicular-to-the cord) image orientation, one advantage of R-L phase encoding is that the SC is less curved along this axis, allowing for a smaller FOV (only if using outer-volume suppression technique) and thus less k-space lines, yielding faster acquisition times in single-line readout schemes and less distortions in EPI. R-L phase encoding also allows for greater robustness in the presence of poor fat suppression (due to the fat in the posterior neck region) and less ghosting due to swallowing and pulsatile vessels. Alternatively, when using EPI, A-P phase encoding will not create a R-L asymmetry, which could be problematic in some study designs where the R-L symmetry of the cord is part of the underlying study hypotheses (e.g. comparing diffusion metrics between the left and right CST). A-P phase encoding is also less prone to peripheral nerve stimulation (although this also depends on the manufacturer, and how oblique the slices are).

Thoraco-lumbar cord

While the present protocol is optimized and validated for the cervical cord, most of the sequences proposed here could be ported to the thoraco-lumbar region with minimal or no adjustments. The amount of modification required mostly depends on the RF receive coil that is available. One notable advantage of the cervical region is the possibility of having coil elements around the neck, which provides better performance for accelerated acquisitions (GRAPPA, SENSE) and higher signal-to-noise ratio (SNR). When imaging the lower cord, coil elements are typically arranged in a flat fashion, reducing acceleration and SNR. Hence, sequences already suffering from low SNR might need modifications, e.g., a larger voxel size.

In general, the T1w, T2w and MT sequences could likely be applied to the lower cord without modifications. The DWI protocol may require additional averaging and/or larger in-plane voxels to increase the SNR. Furthermore, using saturation bands for inner field of view (FOV) DWI acquisitions may be much more challenging or even impossible due to specific absorption rate (SAR) and saturation band thickness limits. The ME-GRE sequence is feasible [74] but may require additional averaging [75], and/or the use of navigator echoes to compensate for respiration-related ghosting. Protocol optimization could be aided by the use of advanced spinal cord phantoms made of "tissue-like" materials that mimic respiration-related dynamic changes in the B_0 field, such as the one proposed by De Tillieux et al. [76].

Other field strengths

While the *spine generic* protocol was optimized and validated at 3T, only slight modifications would be required to adapt the protocol to 1.5T systems. Depending on what researchers would like to do (CSA measurements, lesion quantification, etc.), the SNR and contrast-to-noise ratio would need to be adjusted by finding the right tradeoff between spatial resolution and acquisition time. Relaxation parameters also change at lower and higher fields. For example, tissue T1 is shorter at 1.5T, which could help reduce TR in T1w sequences. Fortunately, SAR is also lower at 1.5T, which allows one to reduce the TR in SAR-intensive sequences, such as the MT protocol or the T2w sequence (including the DWI sequence). Another advantage of 1.5T is that susceptibility distortions on DWI EPI data are reduced.

At 7T, parameters would likely require greater changes than those needed to adapt to 1.5T. While SNR is higher at 7T, allowing one to reduce the voxel size, susceptibility effects are also increased. This is particularly problematic for the EPI-based DWI protocol (increased image distortions) [77] and the long TE gradient echo sequences used for the T2* protocols [78]. Additionally, SAR is higher at 7T, which leads to challenges when using SAR-intensive sequences such as the MT protocol, the DWI sequence, or the T2w sequence.

More challenges exist when moving between field strengths, including B1+ effects, dynamic B_0 changes, changes in T1, T2 and T2*, local vs. body RF transmit coils, and different safety profiles. Further investigations are therefore needed to properly adapt the spine-generic protocol to other field strengths.

Future directions

The *spine generic* acquisition protocol is a major milestone for the SC qMRI community. It provides a starting point for researchers and clinicians implementing new SC imaging initiatives. We would like to stress that the protocol will evolve with new MR hardware and software releases, as well as with research advances such as protocol optimizations and novel pulse sequence developments. Moreover, in future releases, the protocol will also be available for other manufacturers (e.g., Canon). For this reason, we suggest that researchers using and publishing with this protocol always refer to its release number (https://github.com/spine-generic/protocols/releases). The SC MRI community has initiated a forum (https://forum.spinalcordmri.org/) to encourage discussions about the generic protocol, how to use it, and how we could further improve it.

In the Supplementary materials, we discuss alternative techniques to those included in the main procedure (such as advanced shimming, navigator echoes, B1+ mapping, phase sensitive inversion recovery (PSIR), reconstruction, interpolation, and filters), some of which are still at the research stage but could eventually be added to the protocol. In addition, we discuss additional equipment that can be used to immobilize the subject, including cervical collars and custom tight-fitting helmets.

We would like to reiterate that the *spine generic* protocol is not geared towards a specific disease. Researchers are at liberty to tune the proposed protocol by modifying parameters and/or adding/removing sequences as needed. A recent example is the development of a standardized brain and spinal cord MRI protocol for patients with MS [79].

The present study also comes with two publicly-available datasets (single- and multi-subject). To the best of our knowledge, these are the first "large-scale" multi-center qMRI SC datasets ever acquired and made public. The multi-subject dataset could be used to create normative qMRI values, serving as age-matched healthy control references. More generally, these datasets could be used for developing new image processing tools dedicated to the SC, and the fact that they are publically available makes it possible for researchers to compare tools with the same data.

At a time when reproducibility of scientific results is a major concern [80], the proposed consensus acquisition protocol, along with publicly-shared datasets and transparent analysis pipeline, aims to provide a basis for research reproducibility and study harmonization.

Materials

Equipment

MRI Scanner

A whole body GE, Philips or Siemens 3T MRI scanner

Coils

Image quality is largely affected by the receive coil. While most 1.5T and 3T systems use the integrated body coil for radiofrequency transmission to ensure adequate homogeneity, also referred to as the B1+ profile, reception can be done with various other coils, each having specific performance characteristics in terms of their sensitivity profile, which defines signal-to-noise ratio (SNR), and g-factor, which describes the parallel imaging capability; i.e., how much one can accelerate (in the phase-encode and slice-select directions) [5]. The recommended receive coils, for specific parts of the spine, are listed in **Table 3**.

Sequences

The required sequences are illustrated in **Figure 2** and manufacturer-specific sequence names are listed in **Table 2**. All the recommended sequences are available as a product; however, old software versions might not have all up-to-date product sequences, and there may be research sequences that are equivalent. When applicable, this information is mentioned within this manuscript. The protocols (pdf + import files) are freely available at: https://github.com/spine-generic/protocols.

Table 3. Recommended receive coils for SC imaging for GE, Philips and Siemens systems.			
		Cervical	**Thoracic/Lumbar**
GE	**HD/HDxt**	8-ch Cervical Thoracic Lumbar (CTL) array	8-ch CTL array
	PETMR	19-ch Head Neck Unit (HNU) array	14-ch Central Molecular imaging Array (CMA)
	MR750w	16-ch Head Neck Spine (HNS) array	48-ch Geometry Embracing Method Phased Array (GEMPA)
Philips	**Achieva**	16-ch head/neck/neurovascular or 32-ch head coil	15-ch posterior spine(**)
	Ingenia(*)		12-ch posterior array(**)
Siemens	**Trio**	12-ch brain + 4-ch neck array + spine array(**)	Spine array(**)
	Verio		
	Skyra	64-ch head/neck or 20-ch head/neck + spine array(**)	
	Prisma		
	Vida		

Default coils in the spine generic protocol. (*): (i) posterior spine coil could also be used depending on coverage, (ii) for thoracic/lumbar SC imaging; anterior coil could be used to improve image quality in sequences with anterior-posterior phase-encoding. (**): The relevant elements of the spine array are to be selected depending on the region to cover. When using "auto select" (Siemens) or "SmartSelect" (Philips), elements will be automatically selected based on the slice positioning. It is advised to use it. This table is subject to changes with the evolution of the market.

T1w (3D) 1mm - Brain & Spine

T2w (3D) 0.8mm - Cord atrophy

ME-GRE (2D) - Gray matter atrophy

Magnetization Transfer - Demyelination in WM

Diffusion Weighted Imaging - Demyelination in WM - Axon degeneration
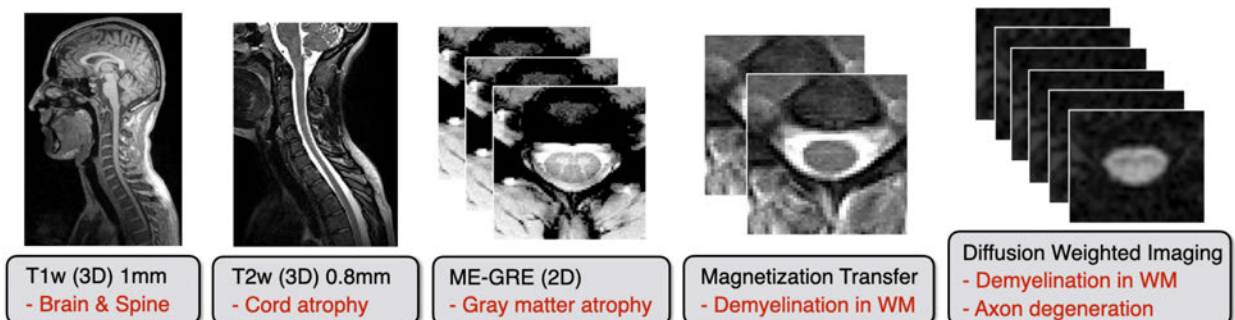
Figure 2. List of sequences included in the spine generic protocol (in black) with possible applications (in red). The total acquisition time is 20-30min, depending on the manufacturer/model.

Procedure

Equipment setup ● TIMING: 2 min

Install coil

1. Select the coil depending on your manufacturer and application (**Table 3**).

Subject and equipment preparation ● TIMING: 5-10 min

Positioning and immobilization strategies.

2. Carefully position the subject to optimize image quality. Try to have the cervical SC as straight as possible, so that axial slices are orthogonal to the SC centerline. This minimizes partial volume effects with the surrounding cerebrospinal fluid (CSF). Reducing neck curvature also helps to improve field homogeneity because the shim volume (i.e., the 3D box centered over the region of interest where the MR system computes the optimal shim coefficients) is less likely to contain air-tissue interfaces. To minimize cervical lordosis, ask the subject to tilt their head slightly towards their chest. Placing some cushions below the head can help, as illustrated in **Figure 3**. However, subjects should not be too uncomfortable and still be able to swallow in a way that minimizes motion. For thoraco-lumbar acquisitions, leg support helps minimize lumbar lordosis and provides more comfort for the subject.

3. Verify that the subject is aligned in the left-right direction and ensure alignment of the spine with the sagittal plane whenever possible.

4. Pad/clamp the subject's head tightly with cushions to avoid head motion. Note that, while doing this has the merit of not requiring additional purchases (e.g. cervical collar[81] or specialized immobilization apparatus), this setup is not easily reproducible and depends on the MR technician. It also does not ensure that subjects are always positioned in the same way for longitudinal experiments. Therefore, it is important that researchers specify the type of cushions used and ideally take a picture showing how to position those cushions while the subject is in the coil.

5. Tell the subject that their neck/spine will be imaged and that if they move, image quality may be severely compromised. Mimic how *not* to swallow by exaggerating head and swallowing motions. Asking subjects not to swallow at all can sometimes lead to more motion due to the swallowing reflex that is triggered once a large volume of saliva is accumulated. This can also pose a choking risk, given that subjects are in a supine position. As a compromise, notify the subject when they can swallow between scans. Ask the subject to breathe normally and to avoid taking deep breaths. Breathing pattern affects image quality due to the dynamic B_0 variations[82] that result from respiration. The latter can cause ghosting on gradient echo data and pixel displacement on EPI sequences.

Pulse Oximeter

6. Install the pulse oximeter on one of the participant's fingers. The pulse oximeter will monitor the cardiac pulse, which will be used for cardiac gating on the DWI scan.

Positioning the Isocenter (laser marking)

7. For thoracic/lumbar applications, set isocenter (laser) around the region of interest. If you are doing brain and cervical cord imaging, mark the isocenter right below the nose. This will ensure that the localizer will cover the desired region. Note that for all other sequences, the table will move so that the center of the FOV is acquired at the scanner's isocenter (to ensure maximal gradient linearity).

Image Acquisition 🔴 TIMING: 20-30 min

CRITICAL Before starting the acquisition, make sure the coil elements are properly selected. If you are using a coil which corresponds to the saved protocol (**Table 3**), the correct elements should be automatically selected. If you are not using a default coil, or if you are acquiring in the thoraco-lumbar region, then you will need to select the elements corresponding to the FOV. For some manufacturers and platforms, the elements will be automatically selected depending on the location and size of the FOV (mode "auto select" or "SmartSelect"), but regardless it is always important to double check.

CRITICAL It is extremely important that you check each image right after its acquisition, not wait until the end of the imaging session. For example, if you notice that the wrong coil was used, fix the problem for the rest of the images (and reacquire the image if there is still time). Or if you spot excessive subject motion, talk to the subject before acquiring the next image.

T1w Scan

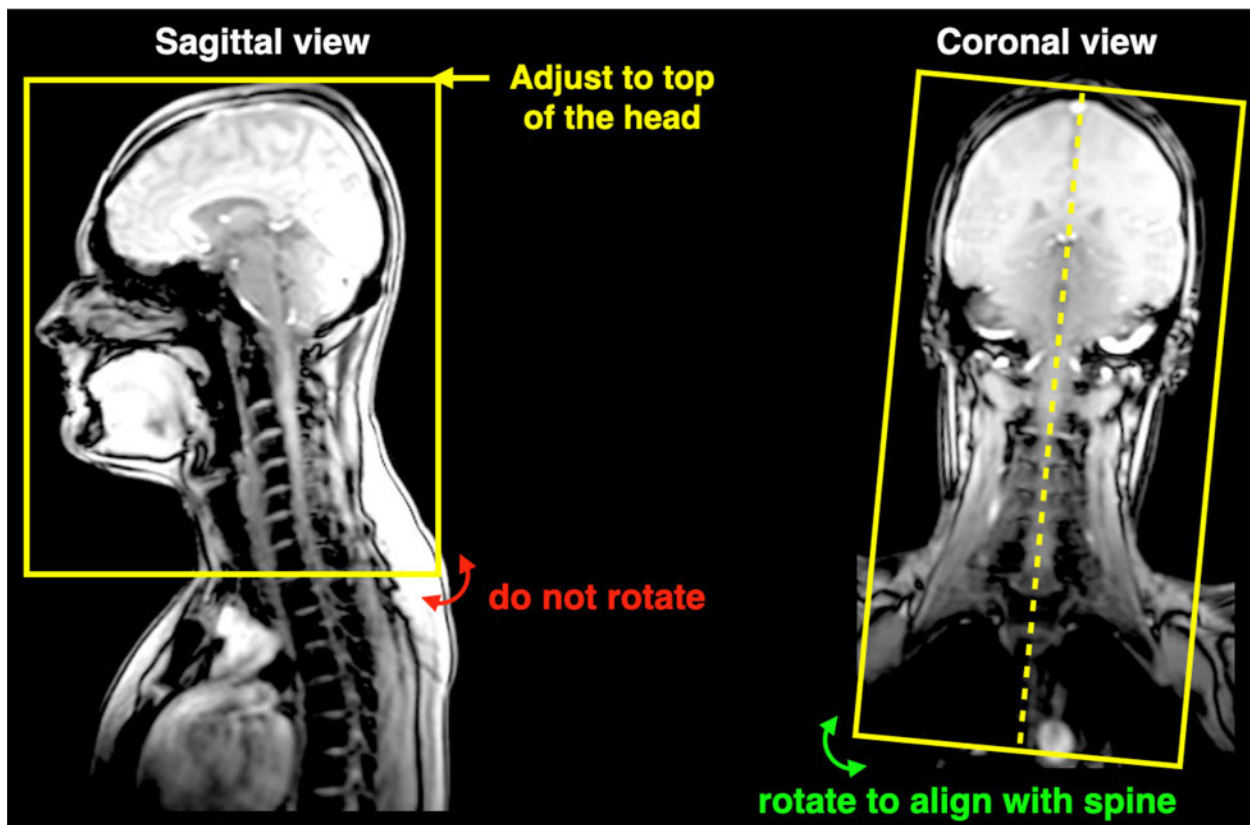8. Adjust the FOV so that it includes the whole head, as shown in **Figure 4**.

Figure 4. Positioning of FOV for T1w scans.

9. GE users: To have the images reconstructed at the proper matrix size, click on "Save Rx → "Scan", then click on "Research" → "Download". Then Click on "Research" → "Display CVs". Then, modify the following CVs accordingly: rhimsize=320, rhrcxres=320, rhrcyres=256. You can check on the console if the field was modified appropriately, by looking at the "image header", after reconstruction. You should get: (0x0028, 0x0010)=192; (0x0028, 0x0030)=1\1.

10. Acquire the T1w scan. Further details of interest about the parameters used in the T1W scan can be found in **Box 1**.

Box 1: Additional details about the parameters for T1w scan

> - **Slab selective excitation:** to avoid R-L aliasing of the body (phase encoding directions on this 3D sequence are R-L and S-I).
> - **TR, TE, TI, Flip Angle:** inspired by the Human Connectome Project (HCP) protocol [83]. The TR was slightly reduced to find a compromise between satisfactory white/gray matter contrast in the brain and reducing the total acquisition time.

T2w Scan

11. Center the FOV at C3-C4 as shown in **Figure 5**. Align along the spine (see coronal view)
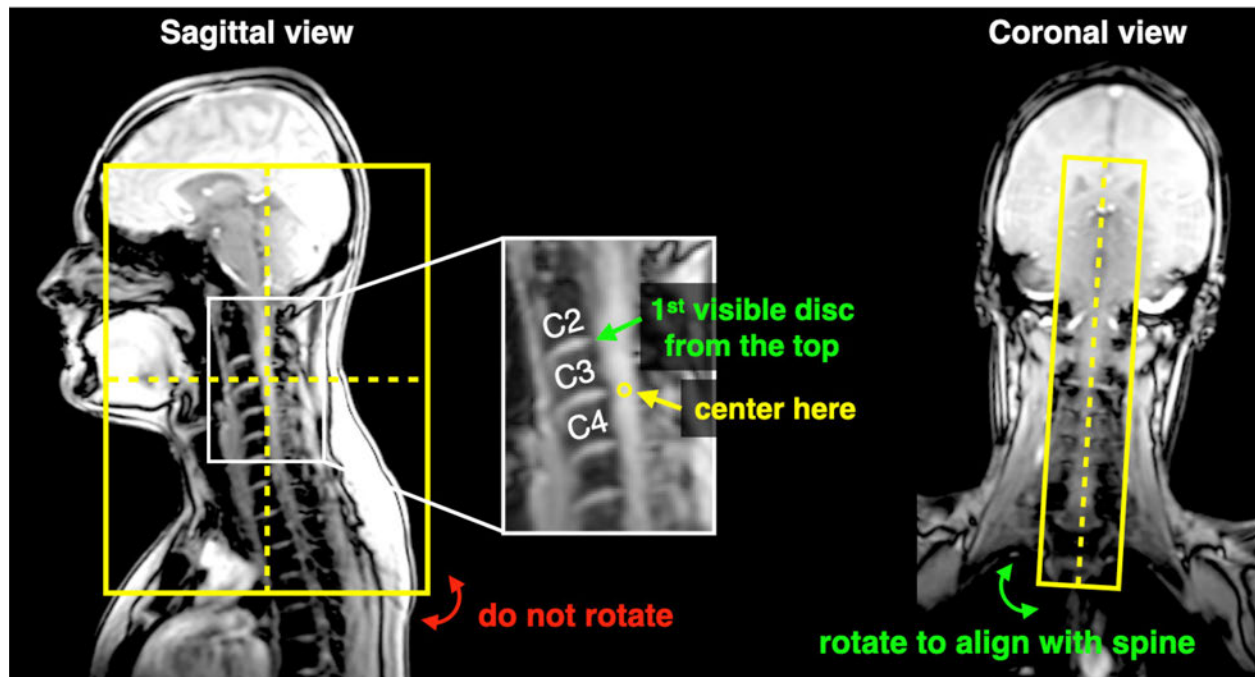
Figure 5. Positioning of FOV for T2w scans.

12. GE users: To have the images reconstructed at the proper matrix size, click on "Save Rx → "Scan", then click on "Research" → "Download". Then Click on "Research" → "Display CVs". Then, modify the following CVs accordingly: rhimsize=320, rhrcxres=256, rhrcyres=256. You can check on the console if the field was modified appropriately, by looking at the "image header", after reconstruction. You should get: (0x0028, 0x0010)=192; (0x0028, 0x0030)=1\1

13. Acquire the T2w scan. Further details of interest about the parameters used in the T2W scan can be found in **Box 2**.

Box 2: Additional details about the parameters for T2w scan:

- **Slab selective excitation:** to avoid R-L aliasing of the body (phase encoding directions on this 3D sequence are R-L and S-I).
- **TR:** sufficiently high to prevent T1 recovery effects causing signal dropout in the CSF (See **Figure 3b** in [33]), while keeping it low to reduce total acquisition time.
- **TE, Flip Angle:** inspired by previous studies [31,64], optimized for satisfactory SC/CSF contrast and SAR.

DWI Scan

14. Use ZOOMit (Siemens), Zoom Diffusion (Philips) or FOCUS (GE), if available. Otherwise, use saturation bands for aliasing suppression (see **Figure 6**).

15. Center the FOV in the cord at the level of C3/C4 disc (**Figure 6**). Rotate the FOV such that slices are orthogonal to the spinal cord, in both the sagittal and coronal planes.
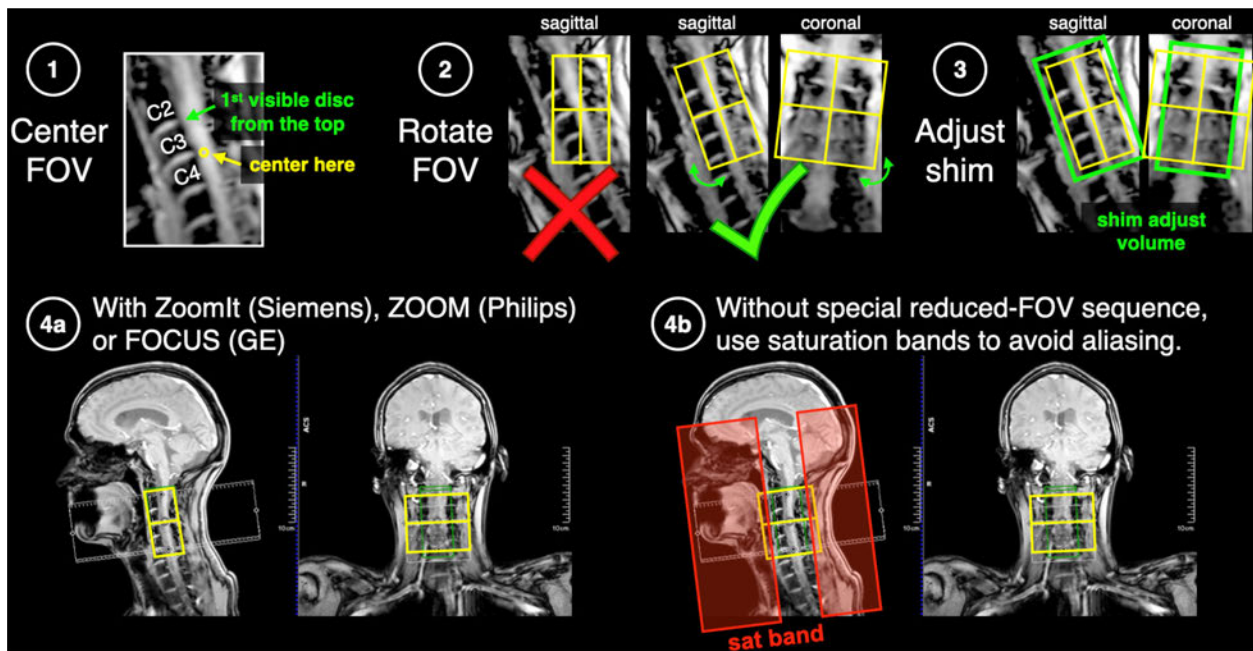
Figure 6. Positioning of FOV, shim box and saturation bands for the DWI scan.

CRITICAL Phase-encode should be A-P.

16. Adjust the shim volume such that it covers the FOV, in both the sagittal and coronal planes (green box).

17. GE users: Click on "shim volume" and then center on the spinal cord. If you cannot modify the size of the shim box, don't worry.

18. GE users: When tilting the slice, the TE might increase by a few ms. If you wish to use the same TE throughout an entire study, we suggest you try tilting the FOV in the coronal and sagittal plane, and report what the minimum TE is. The more you tilt, the longer the TE will be (hence lower SNR) but the more conservative you will be in keeping a fixed TE throughout the entire study.

19. GE users: To have the images reconstructed at the proper matrix size, click on "Save Rx → "Scan", then click on "Research" → "Download". Then Click on "Research" → "Display CVs". Then, modify the following CVs accordingly: rhimsize=96, rhrcxres=86, rhrcyres=43. You can check on the console if the field was modified appropriately, by looking at the "image header", after reconstruction. You should get: (0x0028, 0x0010)=192; (0x0028, 0x0030)=1\1

CRITICAL Before starting the acquisition, make sure the PulseOx trigger is working. It should look like what is shown in **Figure 7**.
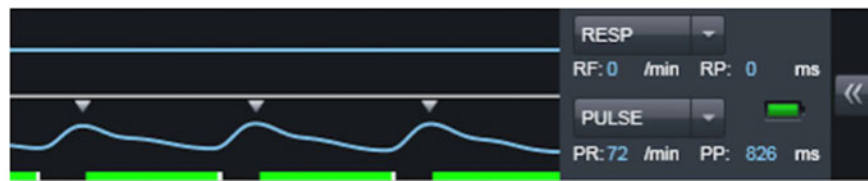
Figure 7. Example of pulse oximeter trace on a Siemens scanner for triggered acquisition (small triangles).

20. Acquire the DWI scan. Further details of interest about the parameters used in the DWI scan can be found in **Box 3**.

Box 3: Additional details about the parameters for DWI scan

- **2D axial**: for spinal tract-based metric quantifications (see section *Slice orientation*)
- **Spatial resolution:** 0.9 x 0.9 x 5 mm (no interpolation)
- **FOV**: Reducing the FOV along the phase-encoding direction for EPI reduces susceptibility-related distortions. SC geometry is favorable to such acquisition techniques. There are three main techniques for reducing the FOV:
  - 2DRF excitation: FOCUS [84] (GE, version DV25 and onwards), ZOOMit [85] (Siemens). Paid licence. Not available on all versions.

- ○ Cross-sectional RF excitations "Zoom Diffusion" [86,87] (Philips): available for software versions 5.3 and higher. For older software, it is possible to use a research sequence which is equivalent to the product sequence.
  - ○ Outer volume suppression with sat bands: (available for all manufacturers). Note: because the saturation band approach is not perfect (fat can be missed and aliased on top of the SC, as exemplified in **Figure 3f** in), it is strongly recommended for it to be used only if other options are not available.
  - ○ For more details about the pros/cons of each reduced FOV technique for the SC, the reader is referred to [88].
- ● **Contiguous slices**
  - ○ Pros: can do tractography, greater statistical power
  - ○ Cons: reduced coverage (more slices can be added at the discretion of the researcher)
- ● **b-value**: single-shell at 800 s/mm^2
  - ○ A single-shell protocol was chosen due to time constraints. For more advanced diffusion models (e.g. NODDI, DBSI), additional shells can be added, potentially increasing TE/TR as the b-value is increased.
  - ○ If the SNR is too low (the SC is barely visible on diffusion-weighted images), the b-value could be lowered (e.g., 600-700 s/mm^2), thereby reducing TE and increasing the SNR. Note that increasing the number of repetitions is not helpful because in this low-SNR regime the noise distribution is more Rician-like, hence averaging of the magnitude signal results in an upward bias. On the other hand, if the SNR is sufficient, on scanners with strong gradients ($\geqslant$80 mT/m) it is recommended to set an additional b-value shell (2000-3000 s/mm^2 or higher) to provide better sensitivity to diffusion-based contrast (to see demyelination/degeneration) and enable the use of more advanced diffusion models. For any multi-shell acquisition, using a fixed TE across shells is recommended.
  - ○ Users should note that a low b-value (800 s/mm^2) may not detect complex fiber geometry for tractography applications (e.g., crossing, fanning). The b-value and number of diffusion directions can be modified to fit researchers' needs.
- ● **Number of directions**: 30-32 uniformly distributed over the sphere. The exact diffusion gradient scheme is manufacturer-specific. The DWI protocol also includes with 5 b=0 images acquired at the beginning or interspersed (this is possible by editing "DiffusionVectors.txt" on Siemens, "dti_vectors_input.txt" on Philips, or "tensor.dat" on GE, but probably only sensible for research sites). All b=0 should have the same TE as the DWI data.
- ● **TR and cardiac gating**: It is recommended to acquire EPI data during the quiescent phase of the cardiac-related SC motion [89]. The quiescent phase of the SC lasts for about 500 ms within a cardiac cycle [89]. On the Siemens platform, we added a concatenation to break down the volume acquisition and only acquire ~3 slices during the quiescent phase of the cord. On the Philips platform, 1 or 2 slices are acquired per beat (depending on the heart rate). We suggest using a pulse oximeter instead of an ECG (it has adequate precision and is less cumbersome to use). The trigger delay is subject-dependent [89] and its definition depends on the platform and sequence parameters, making it difficult to provide an optimal number that fits all subjects and platforms. For example, the SPAIR fat saturation on the

Siemens platform adds ~83 ms before each excitation, while on the Philips platform the minimum delay is about 110 ms (used by the SPIR fat sat pulse and the outer volume suppression pulses). For convenience, we set the delay to the minimum value, but researchers can optimize this value accordingly.

- **TE**: should be minimum (to maximize SNR).
- **Echo spacing** (controlled with the bandwidth): should be minimum (to minimize distortions).
- **Diffusion gradient mode**: monopolar (if available) to ensure lower TE. If needed, bipolar mode can be used to minimize eddy current-related distortions. On older Siemens platforms (e.g. VB17), the ep2d_diff product sequence is bipolar, however research or work-in-progress sequences exist, such as WIP511 (monopolar option, with polarity alternation, freq stab and skewed fat sat).
- **Dynamic Stabilization:** Frequency stabilization (Siemens), Dynamic Stabilization (Philips), Real Time Field Adjustment (GE): These options help reduce artifacts related to changes in the magnetic field over time.
- **Phase Encoding**: P-A instead of A-P so that (i) susceptibility distortions have the effect of "stretching" instead of "compressing" the SC (no information loss) and (ii) in case of poor fat saturation, posterior neck fat will be aliased outside of the FOV.
- **Shimming** box (+ advanced shimming) should be carefully positioned around the SC. See **Figure 7**.
- **Acceleration** (GRAPPA/SENSE): We recommend no in-plane acceleration because a small matrix size (96×96) combined with a reduced FOV (~60% reduction) and partial Fourier (7/8), leaves too few phase-encoding lines for reliable image reconstruction. Besides, in-plane acceleration reduces SNR by factor sqrt(R), where R is the in-plane acceleration factor.
- **Simultaneous multi-slice**: While this technique is gaining popularity for reducing the overall acquisition time by exciting several slices at the same time, thereby reducing the volume TR, we do not suggest its use here because the number of slices (n=15) and their gap is small, which hampers the acceleration performance, and further reducing the TR would hamper longitudinal relaxation.
- **Fat suppression**: 2DRF protocols use water excitation while the Philips Zoom sequence employs a SPIR fat saturation pulse to minimize fat contribution. If insufficient, skewed techniques [90] could be tried.
- **Partial Fourier**: 75% k-space to mitigate phase errors, while still being able to reduce TE. A larger k-space window also minimizes the risk of a total drop-out that can happen when the peak of an echo moves entirely outside the readout window.
- **Fieldmap** (blip-up/down): Given the difficulty of acquiring a robust fieldmap and correcting for susceptibility-related distortions using a blip-up/down sequence in the SC (partly because the manifestation of artifacts in the up/down directions might be slightly different, due to e.g., CSF presence, B_0 field differences between up/down because of respiratory-related B_0 variation), we do not recommend that these be acquired. Any type of correction might introduce more artifacts if misused. Instead, we suggest acquiring data with minimal distortions in the first place (by minimizing the echo spacing, optimizing shimming, etc.) and correcting residual distortions by registering the DWI data on to a structural scan (e.g. b=0

on the T2 space). For more details, see this forum post: http://forum.spinalcordmri.org/t/how-to-correct-for-distortions-in-spinal-cord-diffusion-mri-data/326.

GRE-MT1 / MT0 / T1w Scans

21. Make sure that the FOV center and orientation are the same as for the DWI scan. Normally, if you imported the full protocol, the FOV should be copied automatically from the DWI scan. If not, please do "copy parameters" (center of FOV and orientation). Use "auto" mode for shimming.

22. GE users: To avoid confusion with regards to the slice orientation, the protocol is saved as "axial". Please click on "oblique" to be able to rotate the slice in the sagittal and coronal planes.

23. GE users: To match the RF frequency of other manufacturers, modify the CV `off_rfmt`

24. GE users: To have the images reconstructed at the proper matrix size, click on "Save Rx → "Scan", then click on "Research" → "Download". Then Click on "Research" → "Display CVs". Then, modify the following CVs accordingly: rhimsize=192, rhrcxres=172, rhrcyres=172. You can check on the console if the field was modified appropriately, by looking at the "image header", after reconstruction. You should get: (0x0028, 0x0010)=192; (0x0028, 0x0030)=1\1

CRITICAL If you get a SAR limitation on the MT scan, increase the TR to the minimum suggested (e.g., going from 35 ms to 36 ms). If the TR is increased, it is very important that you also change the TR on the GRE-MT0 sequence (TR should be the same on the MT1 and MT0 scans).

25. Acquire GRE-MT1/MT0/T1w scan. Further details of interest about the parameters used in the GRE-MT1/MT0/T1w scan can be found in **Box 4**.

Box 4: Additional details about the parameters for GRE-MT1 / MT0 / T1w Scans:

- **2D vs. 3D**: 3D is recommended because with some manufacturers (incl. Siemens) the MT pulse is not selective, therefore using a 2D sequence will result in a different MT effect across slices.
- **TR and Flip angle**: optimized so as to minimize the standard deviation of the MTR, given the limitations on different systems (ex: SAR, TR, etc.).
- **TE:** minimized to reduce T2* relaxation.
- **Saturation bands**: not recommended because the offset excitation creates an MT effect, which could vary across manufacturers (different implementation).
- **Fat saturation pulses**: should not be used with a quantitative MT protocol (MTR, MTsat, qMT, MTCSF, etc.) because the off resonance pulse will create an additional MT effect.
- **Water excitation (**using composite binomial pulses): not recommended since the effect on the off-resonance fat signal will impact the MT effect.
- **MT frequency offset:** Using product sequences, the frequency offset cannot be changed. Siemens and GE use 1.2 kHz while Philips uses 1.1 kHz, which is the recommendation for

the spine generic protocol. If, however, one has access to research sequences that allow changing that parameter, increasing the frequency offset (e.g., to 4kHz) will result in higher WM/GM contrast that could be advantageous when segmenting the GM. The RF strength and pulse pattern for the MT pulse cannot be disclosed here because it is proprietary information of the manufacturers.

● **Multiecho combined:** Although combining echoes provides higher SNR, we do not always recommend it because signal dropout at later echo times could bias MT metrics. Also, on GE systems, it is not possible to use multiecho with the MT pulse.

GRE-ME Scan

26. Make sure that the FOV center and orientation are the same as for the DWI scan. Normally, if you imported the full protocol, the FOV should be copied automatically from the DWI scan. If not, please do "copy parameters" (center of FOV and orientation).

27. Adjust shim box so that it follows the spine as closely as possible (see **Figure 8**).
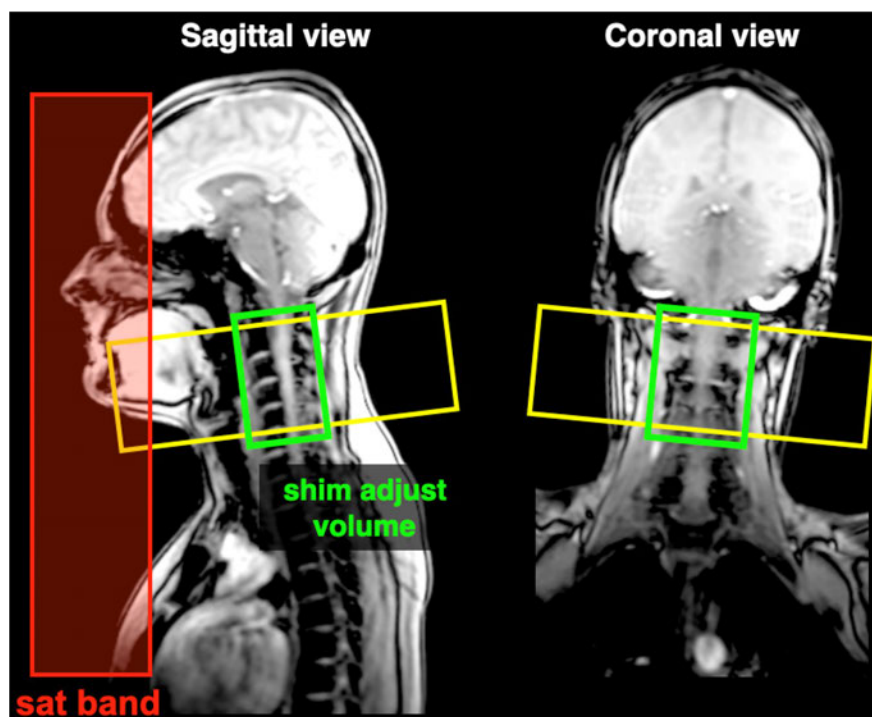
28. GE users: To avoid confusion with regards to the slice orientation, the protocol is saved as "axial". Please click on "oblique" to be able to rotate the slice in the sagittal and coronal planes.

29. GE users: To have the images reconstructed at the proper matrix size, click on "Save Rx → "Scan", then click on "Research" → "Download". Then Click on "Research" → "Display CVs". Then, modify the following CVs accordingly: rhimsize=448, rhrcxres=224, rhrcyres=224.

30. Acquire the GRE-ME scan. Further details of interest about the parameters used in the GRE-ME scan can be found in **Box 5**.

Box 5: Additional details about the parameters for GRE-ME Scan

- **Optimization:** The chosen parameters for this sequence result from a consensus which arose from the "Gray Matter Acquisition Challenge", which was organized during the 5th Spinal Cord MRI workshop [91].
- **2D vs. 3D**: While 3D acquisitions are more SNR efficient, we recommend using 2D acquisitions as they produce "cleaner" images: no aliasing along the 2nd phase encoding direction when using 3D, more homogeneous B1+ profile than 3D acquisition, less sensitive to motion.
- **Spatial resolution:** 0.5 x 0.5 x 5 mm (no interpolation)
- **Saturation band**: adds a slight MT effect due to the off-resonance pulse, which has the effect of slightly increasing white/gray matter contrast. A corollary benefit of this saturation band, positioned coronal and anteriorly (**Figure 8**), is that it also removes signal from a region prone to motion (swallowing and vessel pulsatility in the neck).
- **Monopolar vs. bipolar:** This concerns the filling of k-space across the different echoes. It is more time-efficient to fill the k-space by alternating polarities across echoes, however this leads to a slight inter-echo shift caused by field inhomogeneities. For this reason we recommend using monopolar encoding, with the downside of slightly longer TE and TR.
- **Multiecho combined:** If individual echo images are available; they should be combined during post-processing for more transparency on the aggregation method. MEDIC (Siemens), and MERGE (GE) automatically combine all echoes. The Philips mFFE sequence outputs all the echoes with the option to also output an "accumulated" image, which corresponds to the sum of all echoes. Depending on the version, the MEDIC sequence does not feature the phase stabilization option (navigator-based phase correction which minimizes ghosting), whereas the FLASH does (this depends on the version, e.g.: VE11C does not).

Troubleshooting

Troubleshooting advice can be found in **Table 4**.

Table 4. Troubleshooting table

STEP	PROBLEM	POSSIBLE REASON	SOLUTION
Step 1	Insufficient signal in some parts of the image (**Figure S1**)	**Wrong coil selection:** For each region in the FOV, the proper coil needs to be selected (**Table 3**). For example, if you are planning to cover the head and neck region, then the head/neck coil should be used. In addition, for each sequence, the proper coil elements need to be selected.	If you notice such artifacts in the image, make sure to check those coil parameters.
Steps 2-5	Blurry images (**Figure S2** and **Figure S3**)	**Improper subject positioning:** Proper subject positioning is important both for the subject's comfort (which has an indirect positive impact on image quality) and for the reduction of some artifacts. For example, excessive lordosis can create more pronounced CSF flow and SC motion. **Subject motion:** Subject motion can negatively affect all sequences, with some sequences being particularly sensitive: T1w (step 10), GRE-MT0/MT1/T1w (step 25) and GRE-ME (step 30).	Reposition the subject. Talk to the subject, ask them to not move for the rest of the imaging session. If there is still time before the end of the imaging session, it is recommended to re-acquire the problematic image(s).
Step 3	Misaligned images (**Figure S4**)	**Improper subject/FOV positioning**: If the medial plane of the spine and head is not aligned with the MRI bore, it could lead to subject discomfort and image misalignment when the FOV is not properly rotated about the antero-posterior axis.	Reposition the subject.
Steps 10 (T1w) & 13 (T2w)	Artifact: multiple fine parallel lines adjacent to high-contrast interfaces.	Gibbs ringing	Can be reduced with an apodization filter, e.g. "Raw filter" (Siemens), "Image filter" (Philips).

Step 13 (T2w)	Signal drops in the CSF (**Figure S5**).	**Incorrect acquisition parameter:** Changes to the acquisition parameters can result in undesired artifacts. In the example shown in **Figure S5**, the flip angle was increased, causing the CSF signal to not recover fully (hypointense signal). Other changes in sequence parameters (TR, TE, matrix size, etc.) could also lead to undesired artifacts or biases in the computed qMRI metrics.	Keep the protocol parameters as close as possible to what is prescribed in the spine generic protocol.
Steps 8, 11, 15, 21 & 26	Variable coverage across the studied population.	**Wrong FOV placement:** It is important to follow the prescribed FOV placement, as failure to do so could result in variable coverage across the studied population, and be a source of inconsistencies and biases. **Figure S6** shows an example of wrong FOV placement for a GRE-MT scan.	Keep the FOV as close as possible to what is prescribed in the spine generic protocol.
Step 20 (DWI)	Artifacts on DWI scans (**Figure S7**).	The DWI scan is based on an EPI sequence, which is prone to susceptibility artifacts manifesting as image distortions. Other effects can lead to artifacts when using this sequence, including poor fat saturation and excessive subject or pulsatile motion.	**Poor fat saturation:** This can cause fat to overlay on the SC (see **Figure 3f** in [33]): The cause is likely related to poor shimming. In this case, try to move the table, re-shim, and/or try other fat saturation methods (e.g. frequency-selective, inversion-recovery). If saturation bands are used, look for poorly saturated signals in the saturation band region by prescribing full FOV and looking at the area where saturation bands are located. If the signal outside the FOV is too high, causing it to alias over the SC, try to increase the number of phase encode lines (this will cause slightly more distortions) or to unselect coil elements if they are not necessary (e.g., switching off the anterior neck element).
Step 25 (MT)	Blurry slice edges.	The 3D excitation does not have a sharp profile at the edges.	Discard 2-3 slices at each edge.
Step 30 (GRE-ME)	Signal dropout.	Signal dropout can be caused by intravoxel dephasing.	If you notice substantial signal dropout, try: reshimming, using thinner slices, or reducing the TE (and/or number of echoes).

Anticipated Results

In this section we show images of the same subject acquired across the three manufacturers. Additional examples of good quality data with interactive 3D visualization are shown in the spine generic website (https://spine-generic.rtfd.io/en/latest/data-acquisition.html#example-of-datasets). The interactive embedding in the website is powered by Brainsprite (https://brainsprite.github.io/).

Good quality T1w scans (steps 8-10)

Figure 9 illustrates what good quality T1w scans for all three manufacturers look like. All scans are devoid of any motion artifacts and the signal is homogeneous throughout the SC. The SC is nicely visible in the medial sagittal plane.
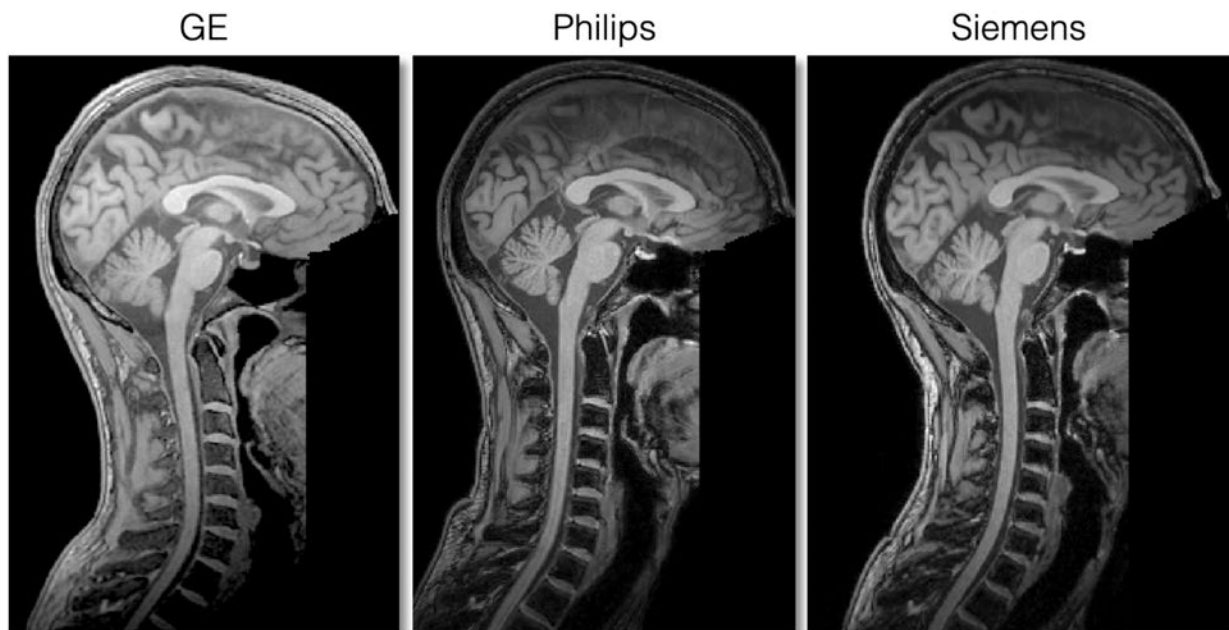
Figure 9. Sagittal views of good quality T1w scans for each manufacturer.

Good quality T2w scans (steps 11-13)

In **Figure 10,** we show good quality T2w scans for all three manufacturers. All scans are devoid of any motion artifacts and the signal is homogeneous throughout the SC. Like for the T1w scans, the SC is nicely visible in the medial sagittal plane.

Figure 10. Sagittal views of good quality T2w scans for each manufacturer.

Good quality DWI scans (steps 14-20)

In **Figure 11** we show good quality DW scans for all three manufacturers. These DW images correspond to a diffusion gradient vector fairly orthogonal to the cord axis, hence the visible spinal cord. When the diffusion gradient is oriented quasi-parallel to the cord, the signal in the cord almost vanishes. Notice the different noise patterns across the manufacturers, which is due to the different types of filters applied. These filters were present in the old version of the protocol but removed in the latest version.
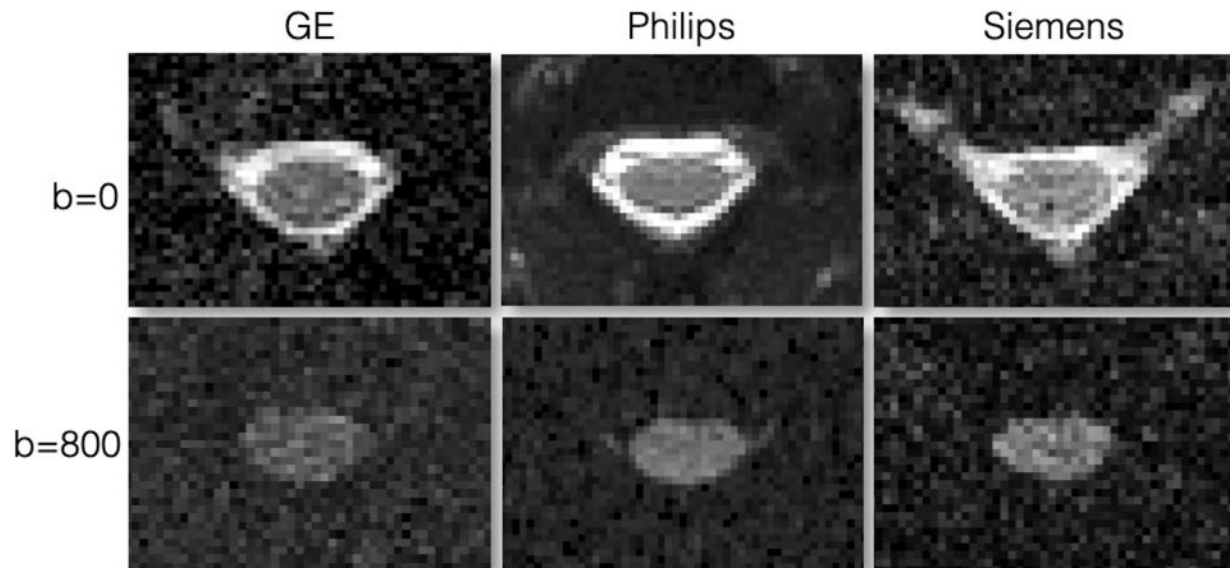
Figure 11. Axial views of good quality data for DWI scans at b=0 s/mm^2 (top row) and b=800 s/mm^2 (bottom row). The DW image corresponds to a diffusion gradient vector fairly orthogonal to the cord axis, hence the visible spinal cord. Notice the different noise patterns across the manufacturers, which is due to the different types of filters applied across manufacturers; these filters were present in an older version of the protocol, but have been removed in the latest version of the protocol in order to minimize differences across manufacturers.

Good quality MT scans (steps 21-25)

Figure 12 illustrates good quality MT0, MT1 and T1w scans for all three manufacturers. Notice the slight motion artifact on the Philips MT0 scan. Also notice the strong signal intensity at the periphery of the tissue on the Siemens scans, which is due to the inactivation of the intensity bias filter. This filter is not relevant when computing qMRI metrics such as MTR or MTsat.
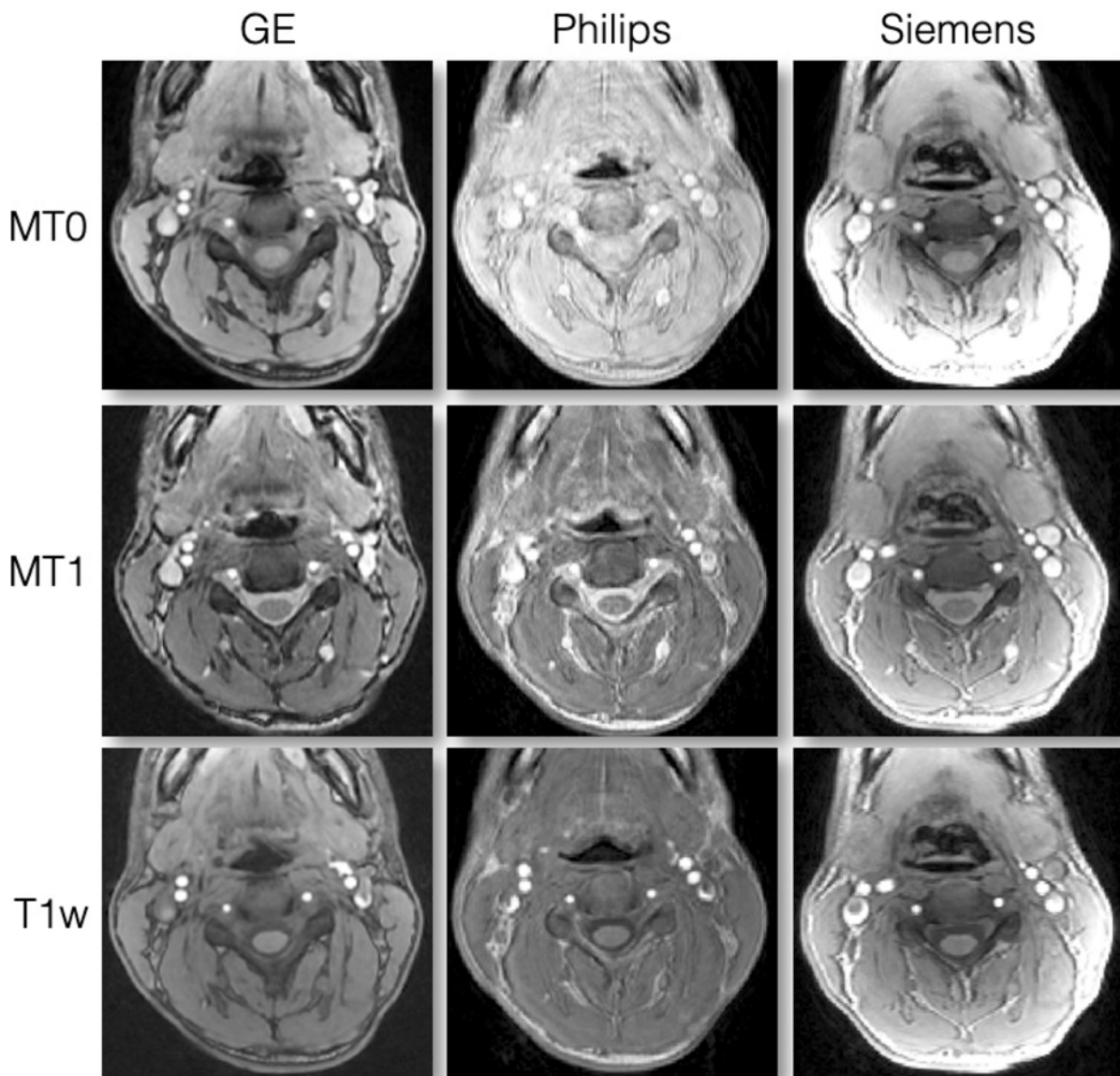
Figure 12. Axial views of good quality data for MT0, MT1 and T1w scans. Notice the slight motion artifact on the Philips MT0 scan. Also notice the strong signal intensity at the periphery of the tissue on the Siemens scans, which is due to the inactivation of the intensity bias filter. This filter is not relevant when computing qMRI metrics such as MTR or MTsat.

Good quality ME-GRE scans (steps 26-30)

In **Figure 13,** we show good quality ME-GRE scans for the three manufacturers. The contrast between GM and WM is good and there is no visible ghosting or signal dropout.
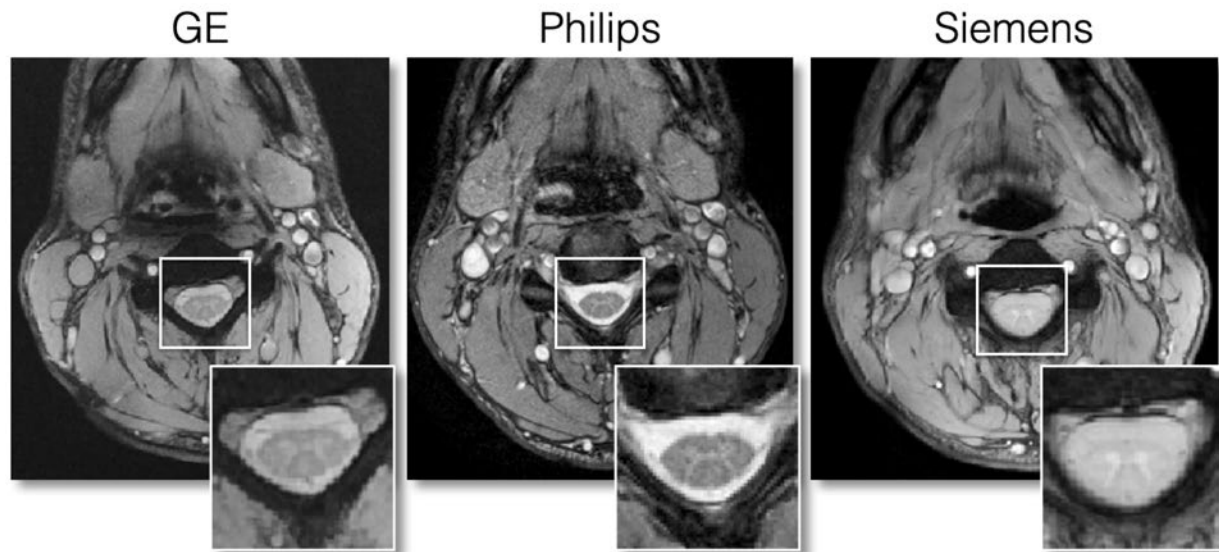
Figure 13. Axial views of good quality ME-GRE scans for each manufacturer.

Acknowledgments

Competing interests: Guillaume Gilbert is an employee of Philips Healthcare.

References

1. Cercignani, M., Dowell, N. G. & Tofts, P. S. *Quantitative MRI of the Brain: Principles of Physical Measurement, Second edition*. (CRC Press, 2018).

2. Cohen-Adad, J. & Wheeler-Kingshott, C. Quantitative MRI of the Spinal Cord. (2014).

3. Wheeler-Kingshott, C. A. *et al.* The current state-of-the-art of spinal cord imaging: applications. *Neuroimage* **84**, 1082–1093 (2014).

4. Stroman, P. W. *et al.* The current state-of-the-art of spinal cord imaging: methods. *Neuroimage* **84**, 1070–1081 (2014).

5. Cohen-Adad, J. & Wald, L. L. Array Coils. in *Quantitative MRI of the Spinal Cord* 59–67 (2014).

6. Barry, R. L., Vannesjo, S. J., By, S., Gore, J. C. & Smith, S. A. Spinal cord MRI at 7T. *Neuroimage* **168**, 437–451 (2018).

7. Saritas, E. U., Holdsworth, S. J. & Bammer, R. Susceptibility artifacts. *In: Quantitative MRI of the Spinal Cord, Elsevier, J. Cohen-Adad and CAM Wheeler-Kingshott, eds.* 91–104 (2014).

8. Bonati, U. *et al.* Cervical cord and brain grey matter atrophy independently associate with long-term MS disability. *J. Neurol. Neurosurg. Psychiatry* **82**, 471–472 (2011).

9. Cohen, A. B. *et al.* The relationships among MRI-defined spinal cord involvement, brain involvement, and disability in multiple sclerosis. *J. Neuroimaging* **22**, 122–128 (2012).

10. Kearney, H. *et al.* Magnetic resonance imaging correlates of physical disability in relapse onset multiple sclerosis of long disease duration. *Mult. Scler.* **20**, 72–80 (2014).

11. Lukas, C. *et al.* Relevance of spinal cord abnormalities to clinical disability in multiple sclerosis: MR imaging findings in a large cohort of patients. *Radiology* **269**, 542–552 (2013).

12. Branco, L. M. T. *et al.* Spinal cord atrophy correlates with disease duration and severity in amyotrophic lateral sclerosis. *Amyotroph. Lateral Scler. Frontotemporal Degener.* **15**, 93–97 (2014).

13. El Mendili, M.-M. *et al.* Multi-parametric spinal cord MRI as potential progression marker in amyotrophic lateral sclerosis. *PLoS One* **9**, e95516 (2014).

14. de Albuquerque, M. *et al.* Longitudinal evaluation of cerebral and spinal cord damage in Amyotrophic Lateral Sclerosis. *Neuroimage Clin* **14**, 269–276 (2017).

15. Querin, G. *et al.* Spinal cord multi-parametric magnetic resonance imaging for survival prediction in amyotrophic lateral sclerosis. *Eur. J. Neurol.* **24**, 1040–1046 (2017).

16. Paquin, M.-Ê. *et al.* Spinal Cord Gray Matter Atrophy in Amyotrophic Lateral Sclerosis. *AJNR Am. J. Neuroradiol.* **39**, 184–192 (2018).

17. van de Stadt, S. I. W. *et al.* Spinal cord atrophy as a measure of severity of myelopathy in adrenoleukodystrophy. *J. Inherit. Metab. Dis.* **43**, 852–860 (2020).

18. Kadanka, Z., Jr *et al.* Predictors of symptomatic myelopathy in degenerative cervical spinal cord compression. *Brain Behav.* **7**, e00797 (2017).

19. Seif, M. *et al.* Cervical Cord Neurodegeneration in Traumatic and Non-Traumatic Spinal Cord Injury. *J. Neurotrauma* **37**, 860–867 (2020).

20. De Leener, B. *et al.* SCT: Spinal Cord Toolbox, an open-source software for processing spinal cord MRI data. *Neuroimage* **145**, 24–43 (2017).

21. Rasoanandrianina, H. *et al.* Region-specific impairment of the cervical spinal cord (SC) in amyotrophic lateral sclerosis: A preliminary study using SC templates and quantitative MRI (diffusion tensor imaging/inhomogeneous magnetization transfer). *NMR Biomed.* **30**, e3801 (2017).

22. Martin, A. R. *et al.* Translating state-of-the-art spinal cord MRI techniques to clinical use: A systematic review of clinical studies utilizing DTI, MT, MWF, MRS, and fMRI. *Neuroimage Clin* **10**, 192–238 (2016).

23. David, G. *et al.* Traumatic and nontraumatic spinal cord injury: pathological insights from neuroimaging. *Nature Reviews Neurology* vol. 15 718–731 (2019).

24. Cadotte, D. W., Akbar, M. A., Fehlings, M. G., Stroman, P. W. & Cohen-Adad, J. What Has Been Learned from Magnetic Resonance Imaging Examination of the Injured Human Spinal Cord: A Canadian Perspective. *J. Neurotrauma* **35**, 1942–1957 (2018).

25. Huffnagel, I. C. *et al.* Longitudinal diffusion MRI as surrogate outcome measure for myelopathy in adrenoleukodystrophy. *Neurology* **93**, e2133–e2143 (2019).

26. Martin, A. R. *et al.* Can microstructural MRI detect subclinical tissue injury in subjects with asymptomatic cervical spinal cord compression? A prospective cohort study. *BMJ Open* **8**, e019809 (2018).

27. Labounek, R. *et al.* HARDI-ZOOMit protocol improves specificity to microstructural changes in presymptomatic myelopathy. *Sci. Rep.* **10**, 17529 (2020).

28. Schmierer, K., Scaravilli, F., Altmann, D. R., Barker, G. J. & Miller, D. H. Magnetization transfer ratio and myelin in postmortem multiple sclerosis brain. *Ann. Neurol.* **56**, 407–415 (2004).

29. Fatemi, A. *et al.* Magnetization transfer MRI demonstrates spinal cord abnormalities in adrenomyeloneuropathy. *Neurology* **64**, 1739–1745 (2005).

30. Lema, A. *et al.* A Comparison of Magnetization Transfer Methods to Assess Brain and

Cervical Cord Microstructure in Multiple Sclerosis. *J. Neuroimaging* **27**, 221–226 (2017).

31. Cohen-Adad, J. *et al.* Demyelination and degeneration in the injured human spinal cord detected with diffusion and magnetization transfer MRI. *Neuroimage* **55**, 1024–1033 (2011).

32. Levy, S. *et al.* White matter atlas of the human spinal cord with estimation of partial volume effect. *Neuroimage* **119**, 262–271 (2015).

33. Cohen-Adad, J. *et al.* Open-access quantitative MRI data of the spinal cord and reproducibility across participants, sites and manufacturers. *Sci Data* **8**, 219 (2021).

34. Grussu, F. *et al.* Relevance of time-dependence for clinically viable diffusion imaging of the spinal cord. *Magn. Reson. Med.* **81**, 1247–1264 (2019).

35. Feaster, D. J., Mikulich-Gilbertson, S. & Brincks, A. M. Modeling site effects in the design and analysis of multi-site trials. *Am. J. Drug Alcohol Abuse* **37**, 383–391 (2011).

36. Fratini, M. *et al.* Multiscale Imaging Approach for Studying the Central Nervous System: Methodology and Perspective. *Front. Neurosci.* **14**, 72 (2020).

37. Grussu, F. *et al.* Multi-parametric quantitative in vivo spinal cord MRI with unified signal readout and image denoising. *Neuroimage* **217**, 116884 (2020).

38. Gros, C. *et al.* Automatic segmentation of the spinal cord and intramedullary multiple sclerosis lesions with convolutional neural networks. *Neuroimage* **184**, 901–915 (2019).

39. Papinutto, N. & Henry, R. G. Evaluation of intra-and interscanner reliability of MRI protocols for spinal cord gray matter and total cross-sectional area measurements. *J. Magn. Reson. Imaging* **49**, 1078–1090 (2019).

40. Perone, C. S., Ballester, P., Barros, R. C. & Cohen-Adad, J. Unsupervised domain adaptation for medical imaging segmentation with self-ensembling. *Neuroimage* **194**, 1–11 (2019).

41. Perone, C. S., Calabrese, E. & Cohen-Adad, J. Spinal cord gray matter segmentation using deep dilated convolutions. *Sci. Rep.* **8**, 5966 (2018).

42. Lévy, S. *et al.* Test-retest reliability of myelin imaging in the human spinal cord: Measurement errors versus region- and aging-induced variations. *PLOS ONE* vol. 13 e0189944 (2018).

43. Gros, C. *et al.* Automatic spinal cord localization, robust to MRI contrasts using global curve optimization. *Med. Image Anal.* (2017).

44. Duval, T., Smith, V., Stikov, N., Klawiter, E. C. & Cohen-Adad, J. Scan-rescan of axcaliber, macromolecular tissue volume, and g-ratio in the spinal cord. *Magnetic Resonance in Medicine* vol. 79 2759–2765 (2018).

45. De Leener, B. *et al.* PAM50: Unbiased multimodal template of the brainstem and spinal

cord aligned with the ICBM152 space. *Neuroimage* **165**, 170–179 (2018).

46. Prados, F. *et al.* Spinal cord grey matter segmentation challenge. *Neuroimage* **152**, 312–329 (2017).

47. Leener, B. D. *et al.* Topologically preserving straightening of spinal cord MRI. *Journal of Magnetic Resonance Imaging* vol. 46 1209–1219 (2017).

48. Duval, T. *et al.* g-Ratio weighted imaging of the human spinal cord in vivo. *Neuroimage* **145, Part A**, 11–23 (2017).

49. Dupont, S. M. *et al.* Fully-integrated framework for the segmentation and registration of the spinal cord white and gray matter. *Neuroimage* (2017) doi:10.1016/j.neuroimage.2016.09.026.

50. Papp, D., Smith, A. K., Mariano, R. & Clare, S. High-resolution quantitative maps of magnetisation transfer, R1 and R2* of the cervical spinal cord in clinically feasible acquisition time using vendor-provided sequences. in *Proceedings of the 27th Annual Meeting of ISMRM, Montreal, Canada* 4992 (2019).

51. Vahdat, S. *et al.* Resting-state brain and spinal cord networks in humans are functionally integrated. *PLoS Biol.* **18**, e3000789 (2020).

52. DiNuzzo, M. *et al.* Towards a Standard Pipeline for the Analysis of Human Spinal Cord fMRI Data Series. in *Proceedings of the 27th Annual Meeting of ISMRM, Montreal, Canada* (2019).

53. Moccia, M. *et al.* Longitudinal spinal cord atrophy in multiple sclerosis using the generalized boundary shift integral. *Ann. Neurol.* **86**, 704–713 (2019).

54. Prados, F. *et al.* Generalised boundary shift integral for longitudinal assessment of spinal cord atrophy. *NeuroImage* vol. 209 116489 (2020).

55. Oh, J. *et al.* The Canadian prospective cohort (canproco) study to understand progression in multiple sclerosis: rationale, aims, and study design. in *35th Congress of the European Committee for Treatment and Research in Multiple Sclerosis, Stockholm, Sweden* P753 (2019).

56. Nestrasil, I. *et al.* Cervical spinal cord diffusion MRI and intraspinal space restriction at the occipito-cervical junction in mucopolysacharidoses patients. in *Proceedings of the 27th Annual Meeting of ISMRM, Montreal, Canada* (2019).

57. Querin, G. *et al.* Presymptomatic spinal cord pathology in c9orf72 mutation carriers: A longitudinal neuroimaging study. *Ann. Neurol.* **86**, 158–167 (2019).

58. Querin, G. *et al.* The spinal and cerebral profile of adult spinal-muscular atrophy: A multimodal imaging study. *Neuroimage Clin* **21**, 101618 (2019).

59. Savini, G. *et al.* Pilot study on quantitative cervical cord and muscular MRI in spinal

muscular atrophy: promising biomarkers of disease evolution and treatment? *Front. Neurol.*

60. Martin, A. R. *et al.* Monitoring for myelopathic progression with multiparametric quantitative MRI. *PLoS One* **13**, e0195733 (2018).

61. Martin, A. R. *et al.* A Novel MRI Biomarker of Spinal Cord White Matter Injury: T2*-Weighted White Matter to Gray Matter Signal Intensity Ratio. *AJNR Am. J. Neuroradiol.* **38**, 1266–1273 (2017).

62. Martin, A. R. *et al.* Clinically Feasible Microstructural MRI to Quantify Cervical Spinal Cord Tissue Injury Using DTI, MT, and T2*-Weighted Imaging: Assessment of Normative Data and Reliability. *AJNR Am. J. Neuroradiol.* **38**, 1257–1265 (2017).

63. Karbasforoushan, H., Cohen-Adad, J. & Dewald, J. P. A. Brainstem and spinal cord MRI identifies altered sensorimotor pathways post-stroke. *Nat. Commun.* **10**, 3524 (2019).

64. Seif, M., Gandini Wheeler-Kingshott, C. A., Cohen-Adad, J., Flanders, A. E. & Freund, P. Guidelines for the conduct of clinical trials in spinal cord injury: Neuroimaging biomarkers. *Spinal Cord* **57**, 717–728 (2019).

65. Bagnato, F. *et al.* Imaging Mechanisms of Disease Progression in Multiple Sclerosis: Beyond Brain Atrophy. *J. Neuroimaging* **30**, 251–266 (2020).

66. Tinnermann, A., Büchel, C. & Cohen-Adad, J. Cortico-spinal imaging to study pain. *Neuroimage* **224**, 117439 (2020).

67. Cohen-Adad, J. Microstructural imaging in the spinal cord and validation strategies. *Neuroimage* **182**, 169–183 (2018).

68. Wheeler-Kingshott, C. A. M. G. *et al.* Imaging spinal cord injury and assessing its predictive value - the INSPIRED study. in *Wings for Life Scientific Meeting, Salzburg, Austria* 29 (2017).

69. Song, S. K. *et al.* Demyelination increases radial diffusivity in corpus callosum of mouse brain. *Neuroimage* **26**, 132–140 (2005).

70. Jones, D. K. & Basser, P. J. 'Squashing peanuts and smashing pumpkins': how noise distorts diffusion-weighted MR data. *Magn. Reson. Med.* **52**, 979–993 (2004).

71. Helms, G., Dathe, H., Kallenberg, K. & Dechent, P. High-resolution maps of magnetization transfer with inherent correction for RF inhomogeneity and T1 relaxation obtained from 3D FLASH MRI. *Magn. Reson. Med.* **60**, 1396–1407 (2008).

72. Xu, J. *et al.* Improved in vivo diffusion tensor imaging of human cervical spinal cord. *Neuroimage* **67**, 64–76 (2013).

73. Summers, P. E., Brooks, J. & Cohen-Adad, J. Spinal Cord fMRI. in *Quantitative MRI of the Spinal Cord* (eds. Cohen-Adad, J. & M, W.-K. C. A.) 221–236 (Elsevier, 2014).

74. Fradet, L., Arnoux, P.-J., Ranjeva, J.-P., Petit, Y. & Callot, V. Morphometrics of the entire human spinal cord and spinal canal measured from in vivo high-resolution anatomical magnetic resonance imaging. *Spine* **39**, E262–9 (2014).

75. Yiannakas, M. C., Kakar, P., Hoy, L. R., Miller, D. H. & Wheeler-Kingshott, C. A. M. The use of the lumbosacral enlargement as an intrinsic imaging biomarker: feasibility of grey matter and white matter cross-sectional area measurements using MRI at 3T. *PLoS One* **9**, e105544 (2014).

76. Tillieux, P. D. *et al.* A pneumatic phantom for mimicking respiration-induced artifacts in spinal MRI. *Magnetic Resonance in Medicine* vol. 79 600–605 (2018).

77. Massire, A. *et al.* Feasibility of single-shot multi-level multi-angle diffusion tensor imaging of the human cervical spinal cord at 7T. *Magn. Reson. Med.* **80**, 947–957 (2018).

78. Massire, A. *et al.* High-resolution multi-parametric quantitative magnetic resonance imaging of the human cervical spinal cord at 7T. *Neuroimage* **143**, 58–69 (2016).

79. Li, D. K. B. *et al.* Developing a Universally Useful, Useable and Used Standardized MRI Protocol for Patients with Multiple Sclerosis. in *Proceedings of the 28th Annual Meeting of ISMRM, Sydney, Australia* (2020).

80. Stikov, N., Trzasko, J. D. & Bernstein, M. A. Reproducibility and the future of MRI research. *Magn. Reson. Med.* **82**, 1981–1983 (2019).

81. Yiannakas, M. C. *et al.* Feasibility of grey matter and white matter segmentation of the upper cervical cord in vivo: A pilot study with application to magnetisation transfer measurements. *Neuroimage* **63**, 1054–1059 (2012).

82. Verma, T. & Cohen-Adad, J. Effect of respiration on the B0 field in the human spinal cord at 3T. *Magn. Reson. Med.* **72**, 1629–1636 (2014).

83. Glasser, M. F. *et al.* The minimal preprocessing pipelines for the Human Connectome Project. *Neuroimage* **80**, 105–124 (2013).

84. Saritas, E. U., Cunningham, C. H., Lee, J. H., Han, E. T. & Nishimura, D. G. DWI of the spinal cord with reduced FOV single-shot EPI. *Magn. Reson. Med.* **60**, 468–473 (2008).

85. Finsterbusch, J. High-resolution diffusion tensor imaging with inner field-of-view EPI. *J. Magn. Reson. Imaging* **29**, 987–993 (2009).

86. Wilm, B. J. *et al.* Diffusion-weighted imaging of the entire spinal cord. *NMR Biomed.* **22**, 174–181 (2009).

87. Jeong, E.-K., Kim, S.-E., Guo, J., Kholmovski, E. G. & Parker, D. L. High-resolution DTI with 2D interleaved multislice reduced FOV single-shot diffusion-weighted EPI (2D ss-rFOV-DWEPI). *Magnetic Resonance in Medicine* vol. 54 1575–1579 (2005).

88. Samson, R. S. *et al.* ZOOM or Non-ZOOM? Assessing Spinal Cord Diffusion Tensor

Imaging Protocols for Multi-Centre Studies. *PLoS One* **11**, e0155557 (2016).

89. Summers P. Staempfli T. Jaermann S. Kwiecinski S. Kollias. A Preliminary Study of the Effects of Trigger Timing on Diffusion Tensor Imaging of the Human. *AJNR* **27**, (2006).

90. Pfeuffer, J. *et al.* Zoomed functional imaging in the human brain at 7 Tesla with simultaneous high spatial and high temporal resolution. *Neuroimage* **17**, 272–286 (2002).

91. 5th Spinal Cord MRI Workshop. *http://www.spinalcordmri.org/2018/06/22/workshop.html*.

Key references using this protocol

- Cohen-Adad, J. et al. Open-access quantitative MRI data of the spinal cord and reproducibility across participants, sites and manufacturers. Sci Data 8, 219 (2021).

- Karbasforoushan, H., Cohen-Adad, J. & Dewald, J. P. A. Brainstem and spinal cord MRI identifies altered sensorimotor pathways post-stroke. Nat. Commun. 10, 3524 (2019). DOI: https://doi.org/10.1038/s41467-019-11244-3

- Martin, A. R. et al. Clinically Feasible Microstructural MRI to Quantify Cervical Spinal Cord Tissue Injury Using DTI, MT, and T2*-Weighted Imaging: Assessment of Normative Data and Reliability. AJNR Am. J. Neuroradiol. 38, 1257–1265 (2017). DOI: 10.3174/ajnr.A5163